Characterization of Spintronic Systems using Soft X-Ray Spectroscopy

A Thesis Submitted to the

College of Graduate and Postdoctoral Studies

in Partial Fulfillment of the Requirements

for the degree of Master of Science

in the Department of Physics and Engineering Physics

University of Saskatchewan

Saskatoon

By

Josha Ho

Permission to Use

In presenting this thesis in partial fulfilment of the requirements for a Postgraduate degree from the University of Saskatchewan, I agree that the Libraries of this University may make it freely available for inspection. I further agree that permission for copying of this thesis in any manner, in whole or in part, for scholarly purposes may be granted by the professor or professors who supervised my thesis work or, in their absence, by the Head of the Department or the Dean of the College in which my thesis work was done. It is understood that any copying or publication or use of this thesis or parts thereof for financial gain shall not be allowed without my written permission. It is also understood that due recognition shall be given to me and to the University of Saskatchewan in any scholarly use which may be made of any material in my thesis.

Requests for permission to copy or to make other use of material in this thesis in whole or part should be addressed to:

Head of the Department of Physics
116 Science Place
University of Saskatchewan
Saskatoon, Saskatchewan
Canada
S7N 5E2

Dean
College of Graduate and Postdoctoral Studies
University of Saskatchewan
116 Thorvaldson Building, 110 Science Place
Saskatoon, Saskatchewan S7N 5C9
Canada

Abstract

The subject of this dissertation revolves around soft x-ray spectroscopy of materials doped with $3d$ transition metals . More specifically, investigating the effects of synthesis techniques and the phenomena associated with subtle changes in synthesis technique resulting in key chemical changes. These materials have the potential to bring a new frontier of opportunity within electronic devices and enable critical new technologies.

This investigation is done using two main techniques. Experimentally, spectra are measured using high resolution synchrotron-based techniques, and these spectra are then compared to theoretical calculations to bring insights into the electronic structure, precise location of defect states, and band gap of promising materials for future devices.

Using these techniques, a system based on the semiconductor In_2O_3 is examined first. With the same host material, and varying the $3d$ transition metal additions (Fe, Ni, Co, Mn), this allows the systematic study of a single synthesis technique with the major variable being the dopant atom. Results here show the successful substitution of iron into the host In_2O_3 lattice, with varying secondary states seen with the other three dopants. Notably, oxygen vacancies are found with iron substituting for indium within the structure, prompting a further investigation into these specific lattice defects.

A system based on the semiconductor SnO_2 is examined, now keeping two consistent codopant atoms, but varying the concentration of the Zn and Co additives. Through this, the effects of not only the concentration of the dopants can be seen, but using two atoms creates two distinct defect sites within the material. The ability to shift the location of oxygen vacancies within the material via annealing cycles during synthesis is displayed. Furthermore the dependency of ferromagnetic properties on oxygen vacancies adjacent to cobalt atoms substituting for tin within the lattice is found.

Acknowledgements

Science is inherently a collaborative work, and the work presented here speaks to that. With a experimental team like ours, groups such as beamline scientists and our own research group (the beamteam) were critical in the success here, and I can't stress their contribution enough.

In addition to this, the support of my supervisor, Professor Alexander Moewes cannot be understated. His facilitation and openness is over the length of my degree in addition to his care and attention to his individual students made a truly enjoyable time.

Finally, I'll state my overwhelming appreciation for the work done by our collaborators abroad in synthesizing the samples measured as a part of this work, and the funding agencies which allowed this to happen, including NSERC, the Canadian Research Chair program, the University of Saskatchewan, and Compute Canada. Without all of these pieces to the puzzle, none of this could have happened.

Contents

List of Tables

List of Figures

List of Abbreviations

ALS	Advanced Light Source
CD	Compact Disk
CLS	Canadian Light Source
DFT	Density Functional Theory
DMS	Dilute Magnetic Semiconductor
EXAFS	Extended X-ray Absorption Fine Structure
GGA-PBE	Generalized Gradient Approximation (Perdew-Burke-Ernzerhof)
IPFY	Inverse Partial Fluorescence Yield
PFY	Partial Fluorescence Yield
REIXS	Resonant Elastic and Inelastic X-ray Scattering
RTFM	Room Temperature Ferromagnetism
RXES	Resonant X-ray Emission Spectroscopy
SRIM	Stopping and Range of Ions in Matter
TEY	Total Electron Yield
TM	Transition Metal
WBGS	Wide-Band Gap Semiconductor
XANES	X-ray Absorption Near Edge Structure
XAS	X-ray Absorption Spectroscopy
XEOL	X-Ray Excited Optical Luminescence
XES	X-ray Emission Spectroscopy
XPS	X-Ray Photoelectron Spectroscopy

Chapter 1

Introduction

In 1880, Alexander Graham Bell introduced the "Photophone", a device that allowed the transmission of sound on a beam of light. In the years since then, optical fiber and optical communications have become a high bandwidth, low interference transmission method, and is the preferred technology for long distance transmission of information [3]. Today, society transmits hundreds of terabits per second over the internet, consuming 9% of global electricity [4]. Fiber optics are just one modern utilization of transmitting information using light. From optical interconnects inside of your computer to the usage of Compact Discs (CDs) to store information light is an exceedingly important tool in communications and technology.

Though this is the basis for much of today's technological infrastructure, information density is only increasing at a rapid pace, and with it, energy consumption. The Cisco Visual Networking Index predicts that global IP traffic will increase from 96 billion Gigabytes per month in 2016 to 278 billion Gigabytes per month by 2021 [5]. As with the switch from Floppy Disks to CDs in the late 1980s changed the way data was stored, there is still a huge potential to change the way data is transferred around the world.

All of this optical communication technology is based upon the duration, frequency, and intensity of the light used in transmission, ignoring the optical polarization. Optical polarization is a familiar concept from sunglasses and modern 3D movies, but by integrating it into data transmission an entirely new channel of information becomes available [6, 7]. In order to facilitate this, new materials are necessary that will allow the control of this optical polarization and more specifically translate the polarization into something easily implemented in a circuit. For these new materials, we begin by investigating the most influential materials of our time–semiconductors.

1.1 Semiconductors

Semiconductors are materials whose conductivity lies between that of a conductor and an insulator. The most widespread semiconductor would be the ubiquitous silicon. With four valence electrons, silicon forms a lattice structure of covalent bonds and with sufficient energy, a free electron can be displaced from a parent atom. The "hole" that is left behind on the parent atom attracts neighbouring electrons due to the net positive charge, and by this electron-hole recombination process a positive charge carrier can propagate through a crystal structure and conduct electrical current [8].

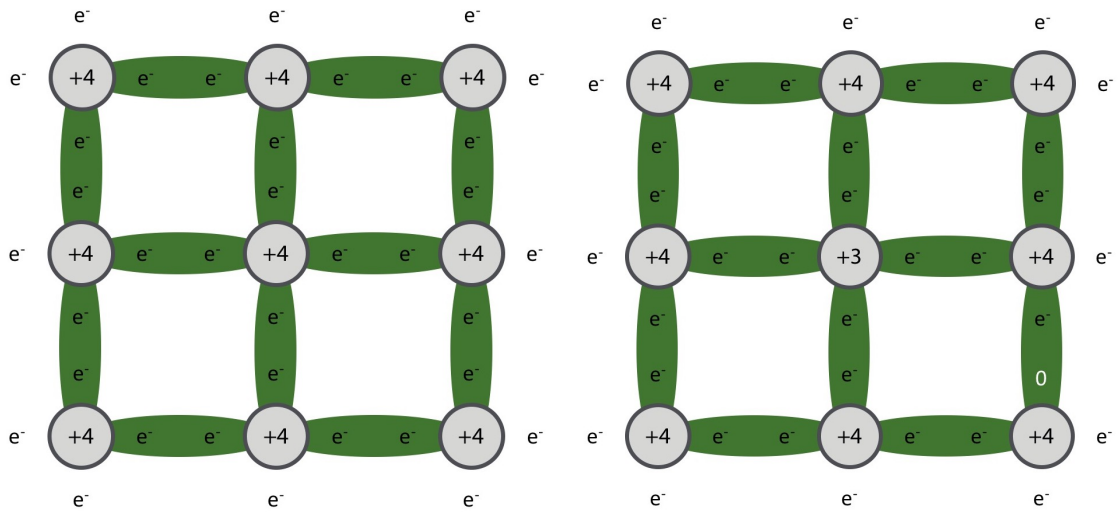

Figure 1.1: An undoped semiconductor lattice (left) and n-type semiconductor (right). The difference in valence between the impurity and host atoms causes the impurity to act as a negative charge donor to the material.

To tune the properties of semiconductors, impurity atoms can be introduced into a semiconductor to increase the concentration of free electrons (an n-type semiconductor) or holes (a p-type semiconductor). This is most often done with elements with a valence ± 1 of the host atoms. The impurity atom acts as an acceptor or donor of negative charge to the material. For example, the addition of boron to a silicon structure (with boron's 3+ valence charge to the 4+ valence charge of silicon) will create an p-type semiconductor with the boron acting as a negative charge acceptor.

The defining characteristic of a semiconductor is the *band gap*; the energy difference

between conduction and valence bands. This band gap is the energy required to promote a valence electron to the conduction band and in turn generate an electron-hole pair. This produces subsequent conduction in a semiconductor. For crystalline silicon, the band gap is 1.12 eV, and for the *wide-band gap semiconductors* (WBGSs) focused on here, the band gap ranges from 2–4 eV. Wide-band gap semiconductors have grown as a research area of interest for a number of reasons. As the operating power and temperature of a semiconductor increases, the bandgap decreases [9]. This results in the ability of WBGSs to operate at higher temperatures than traditional semiconductors, and in higher power scenarios. In addition, as a semiconductor is modified using dopants, the bandgap of the material changes, and if it sufficiently narrows, the material loses key properties of a semiconductor and approaches that of a metal. Given a functional semiconductor material, these dopants are the second piece of the search for a material that can work as the basis for spintronics. In addition to acting as electron donors or acceptors dopants affect additional properties of the material like band gap shifts or the property discussed here of magnetism.

Three distinct groups of magnetic materials will be examined here: diamagnetic, paramagnetic, and ferromagnetic materials. These can be roughly categorized via their magnetic susceptibility, χ_m.

- Diamagnetism opposes an applied magnetic field, characterized by a small ($\sim 10^{-6}$), negative χ_m. Diamagnetism results from the perturbation of electron orbitals caused by an external field hence no magnetic moment is observed in the absence of an applied field.

- Paramagnetism is characterized by a small, positive χ_m and the presence of randomly oriented magnetic dipole moments within a material. With increasing applied magnetic field, magnetism increases within a paramagnetic material as the orientation of the magnetic moments, and the related electron spin, become further aligned.

- Ferromagnetism is a magnetism that persists even in the absence of an external magnetic field, characterized by a large ($> 10^{-4}$), positive χ_m. Ferromagnetism of a material is attached to a critical temperature at which ferromagnetism is lost, referred to as the Curie temperature, T_C.

Ferromagnetism is the property we are most interested in when investigating spintronic materials. Iron, cobalt, and nickel all display ferromagnetism at room temperature, and are natural choices for dopants that will imbue this property into semiconductors.

The search for materials combining properties of ferromagnets and semiconductors has been going on for some time. Some of the first reported hybrid ferromagnet/semiconductor systems were based on the widespread GaAs with Mn dopants [10]. However, while increasing numbers of systems were found successfully combining these properties at low temperatures, the search for hybrid ferromagnet/semiconductor displaying room temperature ferromagnetism (RTFM) is still ongoing. One key example of displayed room temperature ferromagnetism is the substitution of transition metals into semiconducting oxides dubbed dilute magnetic semiconductors (DMSs), which will be discussed in depth. Prior to this discussion, we examine this subset of transition metals, which will be utilized as dopants within semiconductors.

1.2 3d Transition Metals

The properties of transition metals, and more specifically transition metals in period four of the periodic table (Figure 1.3), have unique properties to investigate within the domain of material science. This group of elements is labeled the "3d transition metals" to correspond to their 3d valence electrons, which are major contributors to their chemical properties, and include the crucial elements of iron, cobalt, and nickel referred to in our ferromagnetism discussion in Section 1. More specifically we discuss the localization of the 3d electrons, why this is of interest, and the techniques necessary to analyze the elements using computational techniques.

The most familiar place to start is in the hydrogen atom. Solving the Schrödinger equation gives solutions pertaining to the four quantum numbers: n, l, m_l, m_s corresponding to the principal, angular, magnetic, and spin quantum numbers. The n and l quantum numbers influence the shape of the radial wavefunctions and the related orbitals (eg. the 3d orbitals have $n = 3$, $l = 2$ seen in Figure 1.2). A key feature of the 3d orbitals, is the lack of nodes, regions where the electron probability is zero. This allows 3d electrons to be spatially closer

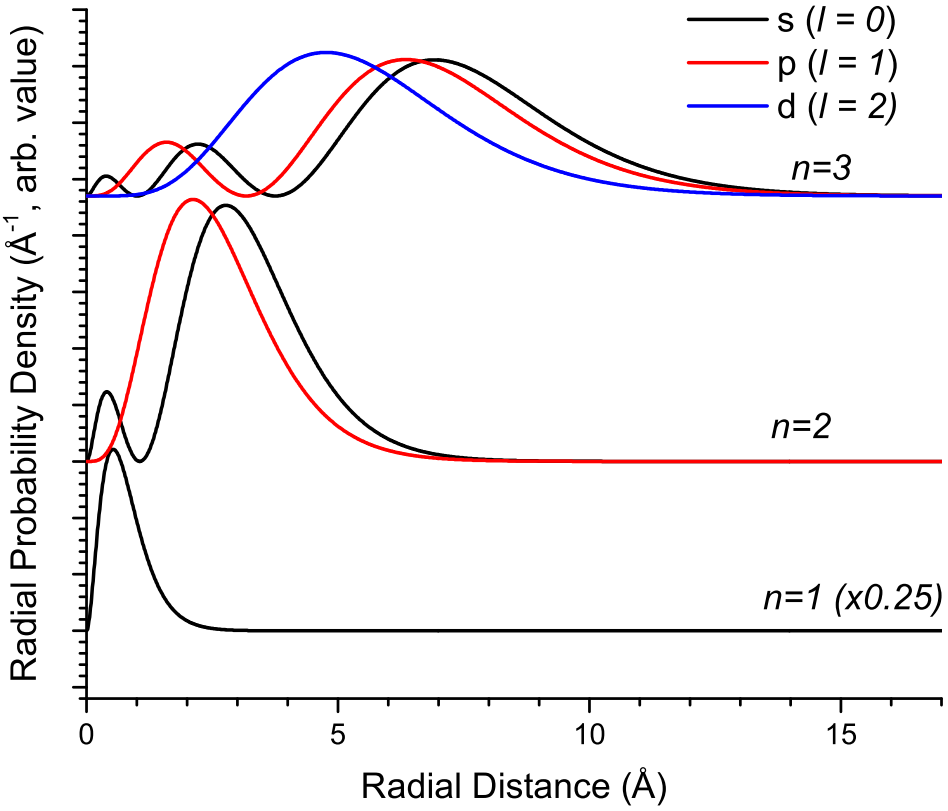

Figure 1.2: s, p, and d radial probability density of orbitals for the hydrogen atom. Here, the absence of nodes within the $3d$ orbitals is clear, one of the main causes of their close spatial proximity to the nucleus.

to the atomic nucleus. Extending this beyond the hydrogen atom, this is a contributor to the oxidation of the $4s$ electrons before the $3d$ electrons in the $3d$ transition metals. This is the basis for the localization of the $3d$ electrons–the strong binding of the $3d$ electrons to the nucleus which affects their binding to neighboring atoms.

One of the major reasons behind these phenomenon is the localization of the $3d$ electrons. We know that the angular wavefunctions of the $3d$ orbitals have distinctive shapes (Figure 1.4). These shapes contribute to electron correlation, the strong interaction between $3d$ electrons due to Coulomb and exchange interactions. Because of this strong interaction and the proximity of the orbitals to the nucleus, the $3d$ transition metals form stretched metal-ligand bonds, which results in relatively weak interactions with surrounding atoms.

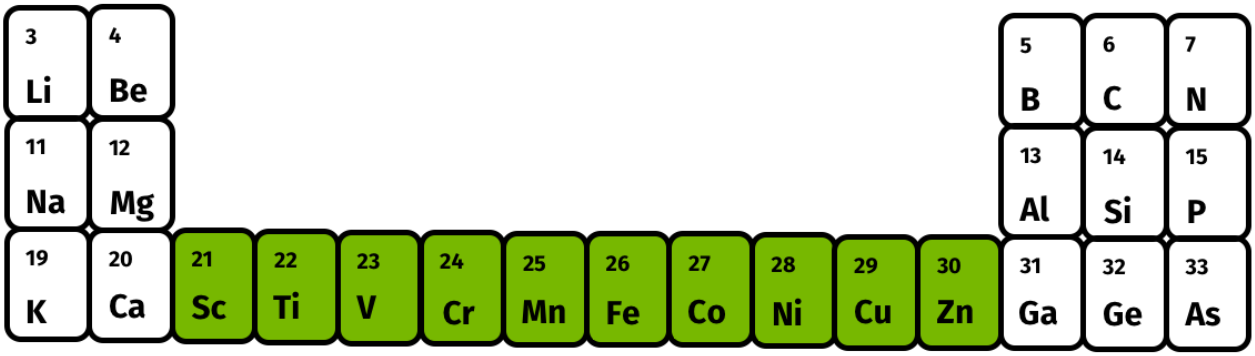

Figure 1.3: Partial periodic table of elements with $3d$ Transition metals highlighted in green.

1.3 Dilute Magnetic Semiconductors

Having discussed the importance of semiconductors to the frontier of technology, and the unique properties of the $3d$ transition metals, the properties of the two when combined is the natural topic to discuss. The idea of a DMS system is just that: combine a non-magnetic semiconductor and transition metal element dopants; with low dopant concentrations, the semiconducting properties of the host semiconductor can be maintained, and magnetic properties can be introduced into the material. This concept has been proven at low temperatures, however the difficulty remains in RTFM–maintaining a meaningful amount of magnetism in a sample at a reasonable operating temperature for commercial use (> 300 K) [12]. Dietl *et al.* predicted via theory a stable high Curie temperature (T_C), for ZnO and GaN. Since both of these are wide bandgap semiconductors, many researchers turned their attention to DMS systems, following the trend of doped WBGSs as promising candidates for DMS systems.

The mechanism producing ferromagnetism in DMS systems is an ongoing debate. This was partially resolved by Green *et al.* in confirming the role of oxygen vacancies within In_2O_3:Fe facilitating the magnetism found in the system [13].

Oxygen vacancies are a common reasoning for many of the abnormal properties in DMS systems. During the synthesis process, oxygen atoms ejected from the lattice can both compensate for charge differences between dopant atoms and the host material, but can also act as electron donors which contributes to overall electron-hole mobility.

A second consideration in the understanding of spintronic properties emerges from in-

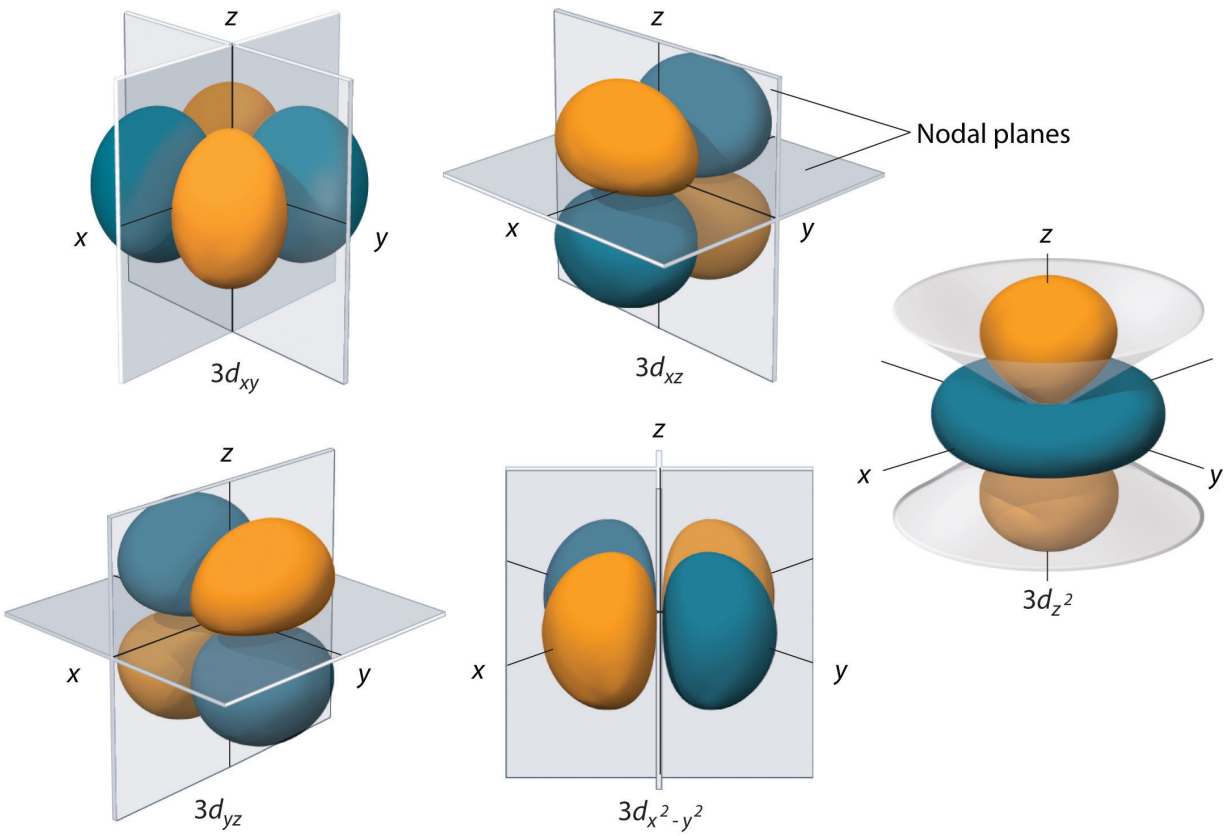

Figure 1.4: Electron distribution for 3*d* orbitals. The geometric orientation and proximity to the nucleus for these contribute to the interesting properties of the 3*d* transition metals. Reprinted from [11] with permission.

consistencies in reported RTFM within DMS systems in the past [14]. This was partially addressed by Garcia *et al.* demonstrating that even ferromagnetic filings from stainless steel tweezers in contact with samples can cause a drastic change in magnetic measurements [15]. This highlights the sensitive nature of the dilute systems under investigation, and the necessity for further study of DMS systems to understand the effects of synthesis methods, dopant concentrations, and experimental procedures to progress the field of DMS systems towards real-world applications.

1.4 Synthesis Methods

In addition to the base material of a DMS system, one of the large topics of discussion is the effect of differing synthesis methodologies to get to the end result. Take, for example, the aforementioned report of a since unmatched magnetic moment of 7.5 ± 0.5 μB/Co within cobalt doped SnO_2. This pulsed-laser thin film sample started the search for room temperature ferromagnetism within a wide range of transition metal dopants within SnO_2 and other host oxides, with the acknowledgement that other factors besides the dopant TM ions are factors in the final magnetic properties of a material.

This becomes a focal element for this discussion, and two synthesis methods are discussed here: ion implantation, and the hydrothermal method. These synthesis methods are demonstrative of two major streams of spintronics research which are necessary stepping stones in our investigation.

1.4.1 Ion Implantation

Ion implantation here references the impingement of ions into thin films via a high current ion source in a vacuum environment. Metal from a cathode is vaporized and a dense plasma is formed; once directed, a radial profile of ions can be directed in a beam towards a given material with an energy on the order of keV. This procedure has the advantage of being independent of the host lattice, and systematic; given a thin-film semiconductor, any ion of choice can be directed towards the material and the effects of the high-energy incorporation studied. Because of this and the inherent self-regulation of the process, ion implantation is the process used in virtually all semiconductor device manufacturing today motivating a structured study of it to work towards device applications [16].

Two things of note during the implantation procedure. Ion implantation can cause significant distortions and secondary defects in the material due to the high energy nature of the reaction usually referred to as "damage". In addition bombardment has a non-uniform depth of incorporation. Both of these can be attributed to the electronic and nuclear stopping interactions between the thin film material and the ions, causing the concentration of ions within a material to vary depending on the distance from the surface as the number of incident ions

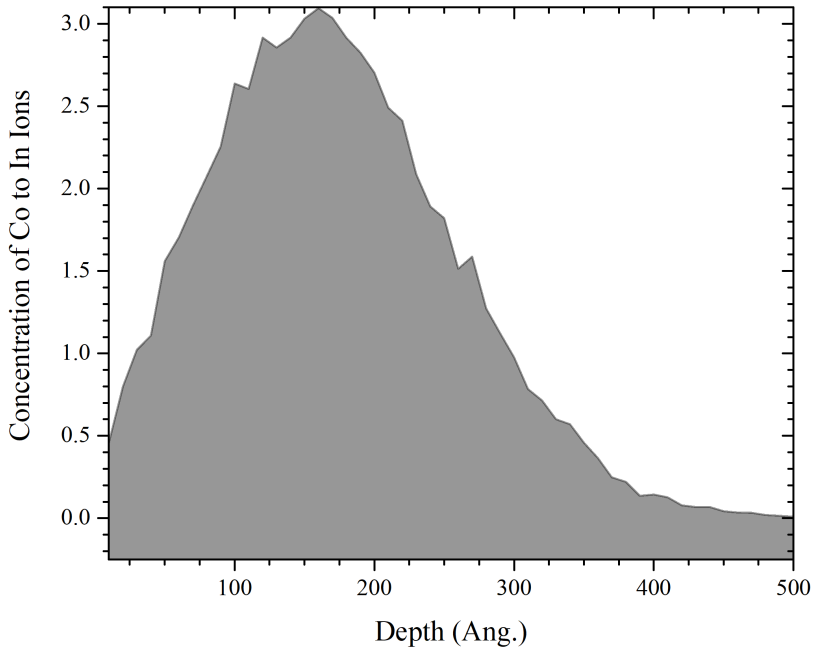

Figure 1.5: Cobalt concentration within ion bombarded In_2O_3, simulated using an ion implantation energy of 30 keV, fluence of 2×10^{17} ions/s $\cdot$ cm^2, and an In_2O_3 density of 6.75 g/cm^3.

present capable of interacting with host ions decreases. In Figure 1.5, the concentration of cobalt within a thin film In_2O_3 sample is seen, demonstrating a peak concentration of 3.1 Co/Sn at $\sim$ 160 Å, but a distinct non-uniformity over the entire sample depth, simulated using the Monte Carlo software "stopping and range of ions in matter" (SRIM) [17].

1.4.2 Hydrothermal Synthesis

Contrasting the secondary doping process of ion bombardment, hydrothermal synthesis creates crystal structures starting from aqueous solutions. This relatively simple procedure requires a multicomponent reaction mixture and high pressures to create highly uniform particles of a desired material [18]. The small particle size of hydrothermal synthesis (on the order of 10-50 nm) provides a high surface to volume ratio, which minimizes any depth-dependent effects in the material, however the inherent nature of a wet synthesis method necessitates high attention to obtain chemical homogeneity within a sample. Hydrothermal

synthesis relies on the crystallization of aqueous solutions at high temperature and pressure within an autoclave. With temperatures ranging from $100 - 500°C$ and pressures ranging from 10-3700 atm, hydrothermal synthesis has a high variation of crystalline morphologies based on these two variables. In the synthesis of spintronic materials where often homogenous materials are investigated, this can be challenging to ensure secondary phases are not occurring within a given material.

Ion implantation is widespread and predictable, but damaging. Hydrothermal synthesis is low cost and decreases depth effects, but risks homogeneity. Here we investigate both methodologies as real-world techniques with the potential to be used towards device applications on a large scale. To do this, we narrow our scope both material-wise and technique-wise to a small subset of spintronic materials applying a battery of highly descriptive synchrotron-based techniques.

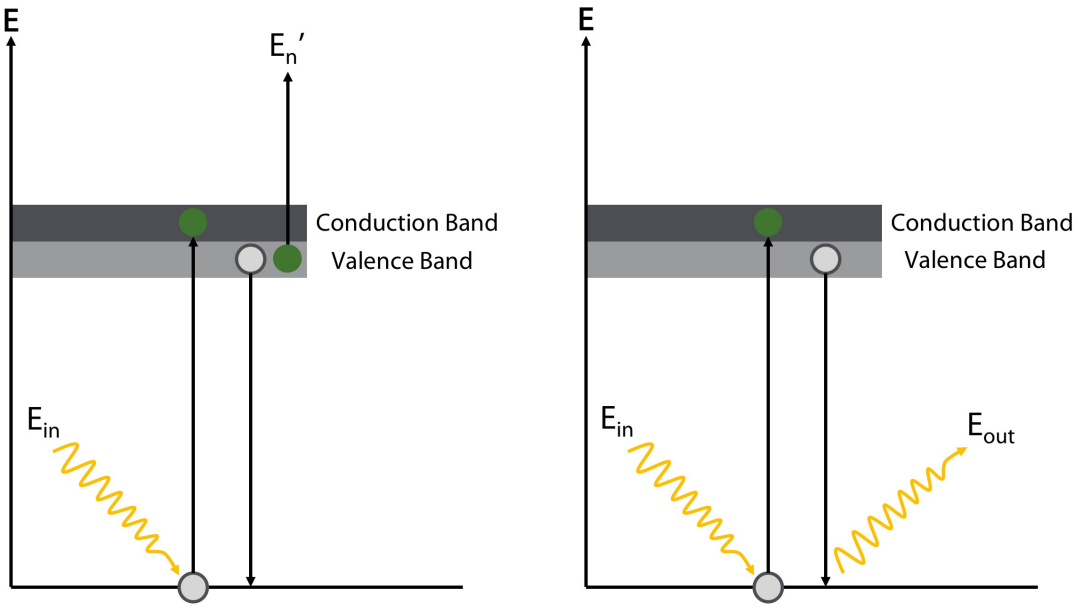

Figure 1.6: Pictorial representation of X-ray absorption spectroscopy excitations, by electron yield detection (left), and fluorescence yield detection (right).

1.5 Experimental Techniques

Synchrotron light sources have provided the powerful experimental resource of high intensity, polarized and most importantly monochromatic light. The advent of this has created a new set of experimental techniques of which a subset will be addressed within here. This subset revolves around the field of soft x-ray spectroscopy. Soft x-rays include the range of energies from 50 eV to 2000 eV and serve a key role in our studies, due to the energy levels of many core levels being found in this range; for our purposes we will focus on the transition metal (Sc, Ti, V, Cr, Mn, Fe, Co, Ni, Cu, and Zn) $2p$ levels and two specific techniques, x-ray absorption spectroscopy and x-ray emission spectroscopy.

1.5.1 X-ray Absorption Spectroscopy

For a given core electron, there is a corresponding energy related to the excitation of this core electron to a higher energy level. When an incident x-ray has an energy greater than

this energy, there is a possibility that the electron is promoted into a state in the conduction band. The probability, $\sigma(\omega)$, for the absorption of a photon follows Fermi's Golden Rule #2,

$$\sigma(\omega) = 4\pi^2\alpha\omega|\left\langle f\right|\epsilon\cdot\mathbf{r}\left|i\right\rangle|^2\delta(E_i+\omega-E_f) \tag{1.1}$$

where ω is the energy of the incident photons, α is the fine structure constant, ϵ is the vector potential of the applied electromagnetic field, $\mathbf{r}$ is the position operator, $|i\rangle$ the initial state with energy E_i, and $\langle f|$ is the final state with energy E_f.

In soft X-ray Absorption Spectroscopy (XAS), we focus on the case when the incident x-ray energy is close to equal with the binding energy of an electron. As the incident x-ray energy is changed across a certain elemental edge, the quantity of x-rays absorbed by a material of interest can be monitored, which allows a direct investigation of the conduction band.

For the given choice of soft XAS on $3d$ transition metals, there are two distinct advantages to the technique: elemental specificity and sensitivity to local coordination.

Each distinct absorbing element is affiliated with characteristic absorption energies corresponding to the binding energies of electron shells. In the soft x-ray range (50-2000 eV), our $3d$ transition metals exhibit characteristic $L_{2,3}$ transition edges with a separation distance of > 40 eV. Since the energy resolution (ΔE) of XAS beamlines for a given photon energy (E) is far more precise than this ($E/\Delta E = 5000$ in our case), information about a single transition metal element even in the presence of another can be obtained.

In addition to this elemental separation, XAS displays the stark contrast in local coordinations of an atom in obtained spectra. That is, due to the contributions of d electrons in close proximity, the fine structure of a spectra change dramatically. In Figure 1.7, experimentally derived spectra with visual comparison to reference samples show a clear Fe^{3+} valence for these materials, with an octahedral coordination, as opposed to the tetrahedral coordination of FeO.

In the soft XAS regime, two methodologies to measure these transitions are used within our study: total electron yield (TEY) and partial florescence yield (PFY). TEY measures the total replenish electrons resulting from the XAS excitation and PFY measures the emitted photons resulting from the relaxation of electrons during the XAS excitation relevant to the

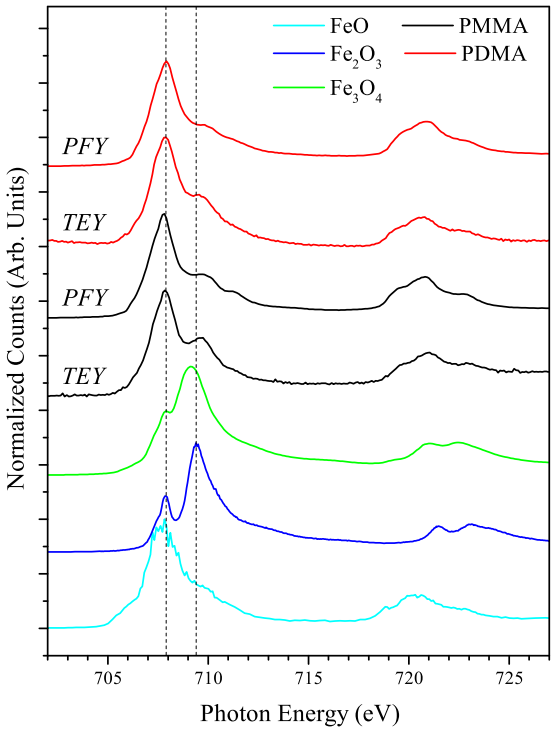

Figure 1.7: Iron $L_{2,3}$ Spectra for Polymethyl Methacrylate based Foldamer samples in comparison to oxide reference samples. Here, the local coordination of the samples is visible without any theoretical calculations.

transitions of interest (Fig. 1.6).

Total electron yield measures the quantity of photoelectrons, Auger electrons, and secondary electrons produced via the excitation of core electrons to states in the conduction band and continuum. This is done via the monitoring of a drain current, replenishing the electrons lost in these processes. Since TEY relies on the quantity of ejected electrons, the mean free path of the electron ($\sim$ 1 nm) limits the probing depth and subsequently the volume of interaction for the measurement. Since only electrons within a shallow depth successfully leave the material, this leads to an inherent surface sensitivity of the TEY technique, which can be valuable in contrasting bulk material properties to surface effects such as oxidation. One of the challenges of this surface sensitivity is the saturation effects that can occur as a result. Depending on the experimental setup and the nature of the sample being measured, if all photons are absorbed within the electron escape depth (that is, all generated electrons escape the material), then the overall absorption coefficient of the material isn't properly

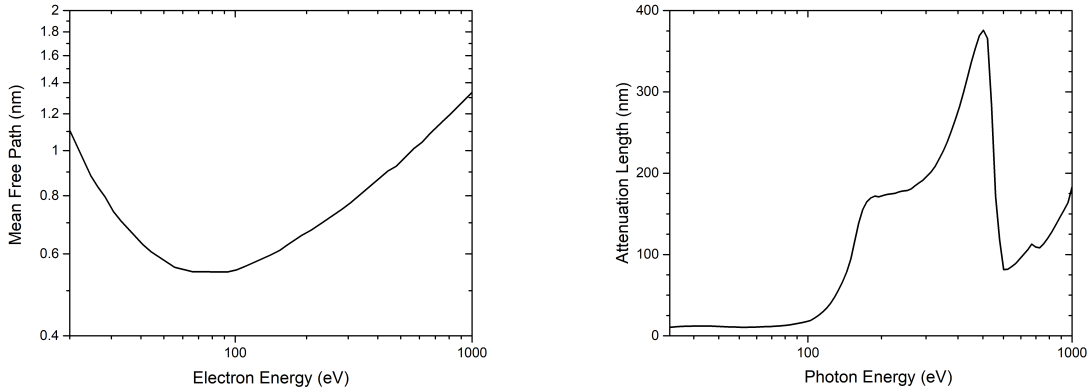

Figure 1.8: Theoretical electron mean free path (left) [1] and x-ray attenuation length for SnO_2 (right) [2].

captured.

Instead of the elecron-based process of TEY, partial fluorescence yield is a photon-in photon-out process. Therefore, the interaction is limited by the photon attenuation length which has been extensively modeled using photoabsorption measurements of elements, and an example is shown in Figure 1.8. Two key features are seen here for SnO_2: Firstly, the attenuation length ($\sim$ 100 nm) is two orders of magnitude higher than our electron mean free path. Secondly, the sharp decrease in the attenuation length near 540 eV can be attributed to the absorption energy of the Oxygen 1s electrons. Similar to electron yield, this has the pitfall of self-absorption effects where all the generated fluorescence photons escape from the sample (once again, not reflecting any absorption occurring).

This concept of fluorescence yield can also in some cases be extended to that of inverse partial fluorescence yield (IPFY), which is robust against self-absorption effects and brings the least amount of experimental distortions due to self-absorption or saturation effects. IPFY relies on the measurement of fluorescence from an element in the material of an energy lower than the absorption edge being investigated. The integration of this fluorescence is inverted, resulting in the absorption cross-section for the edge of interest. However, since changes in this non-resonant fluorescence are significantly smaller than the resonant edge fluorescence, IPFY is often not feasible due to a statistical noise floor [19].

Each of the three, TEY, PFY, and IPFY have experimental considerations which deter-

mine their usability. TEY and PFY can often give information about the surface and bulk properties of a material respectively, demonstrating homogeneity of the sample. IPFY can give the true, undistorted spectra, but requires the existence of a lower absorption energy element present in the material.

Demonstrably, the fluorescence of elements within a material is of great interest, first in the total integrated quantity for the fluorescence yield techniques above. In addition to this, with the high energy resolution provided by modern detectors, the discussion of energy resolved fluorescence brings a second technique in our toolbox – x-ray emission spectroscopy.

1.5.2 X-ray Emission Spectroscopy

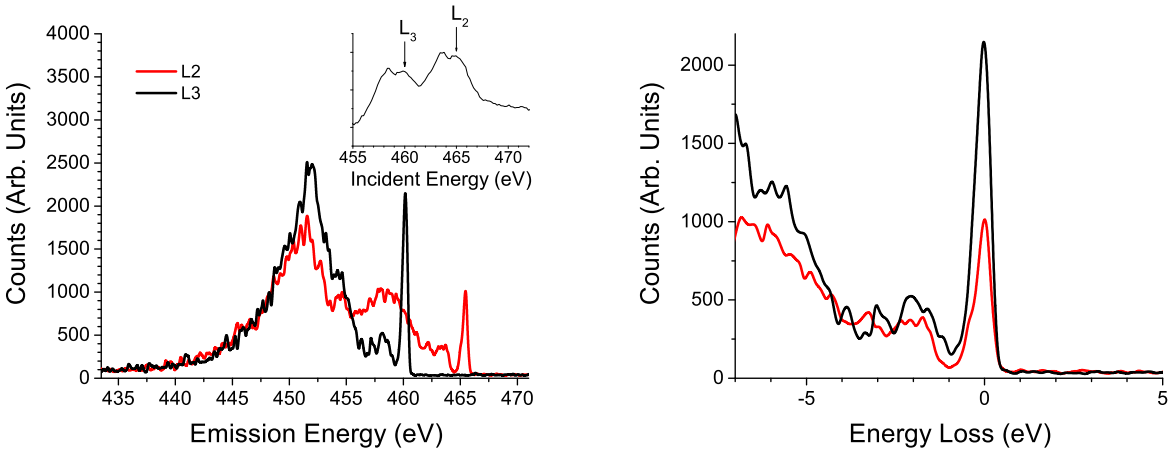

Figure 1.9: RXES spectra for 2D Titanium MXene samples. The emission energy scale (left) accentuates the resonant titanium L_3 emission (the XAS with excitation energies displayed in the inset), where the energy loss scale (right) accentuates the *d*–*d* transitions present in both the L_2 and L_3 spectra.

Here, we focus on the information provided by *resonant* x-ray emission spectroscopy (RXES), the process when the incident x-ray energy is close to the absorption edge of an element. This results in the excitation of an electron to an unoccupied conduction band state, followed by the decay of an occupied state to fill the resultant core hole. RXES creates an electron–hole pair that can propagate through the lattice commonly referred to as an "exciton". This electron–hole pair holds the difference in energy between the incoming and outgoing photon. Practically, by using a fixed incident energy and monitoring the emission

energy, this energy difference can be ascertained, giving a direct probe of the energy required for electron transport within the material. The *d*–*d* excitations, the energy difference resulting from an electron being able to occupy many different orbitals, is a key phenomenon able to be investigated by XES that cannot be measured via optical spectroscopy.

We can describe the RXES process via the Kramer-Heisenberg formula,

$$F(\Omega,\omega) = \sum_j \left| \sum_i \frac{\langle j| T_2 |i\rangle \langle i| T_1 |g\rangle}{E_g + \hbar\Omega - E_i + i\Gamma_i} \right|^2 \delta(E_g + \hbar\Omega - E_j - \hbar\omega) \tag{1.2}$$

defining incident and outgoing photon energies of $\hbar\Omega$ and $\hbar\omega$ transition operators T_1, T_2 ($T_i = \epsilon_{\mathbf{i}} \cdot \mathbf{r}_{\mathbf{i}}$ under the dipole approximation) and a core state lifetime Γ_i. A key component of this is in addition to initial and final states $|g\rangle$ and $|j\rangle$, the intermediate state $|i\rangle$ is included. The two matrix elements describe the two step process describes both the creation of a core hole state from the ground state and the subsequent emission process.

XAS is sensitive to the oxidation states and local coordination of an element and RXES is sensitive to covalent interactions – in our case, ligand-to-metal charge transfer (CT) excitations.

The photon emission in Figure 1.6 is inherently energy resolved, as discussed in Section 1.5.1. In RXES, the spectrometer can allow the investigation of a highly resolved emission spectra.

1.5.3 X-ray Excited Optical Luminescence

X-ray excited optical luminescence (XEOL) differs from the techniques above as an x-ray photon-in *optical* photon-out process directly resulting from the excitation that is occurring during XAS. However, instead of examining a state in the conduction band or valence band like XAS or XES, the energy lost through the emission of visible light can be monitored that is the result of electron-hole recombinations. The first, and rather obvious advantage of XEOL is the usage of x-ray photons as an excitation source. Through this, any affects on the measured spectra from scattered incoming photons can be effectively removed.

Secondly is that while XEOL is related to UV-excited photoluminescence experiments, it is inherently different in the population by energy transfer of excited core electrons as

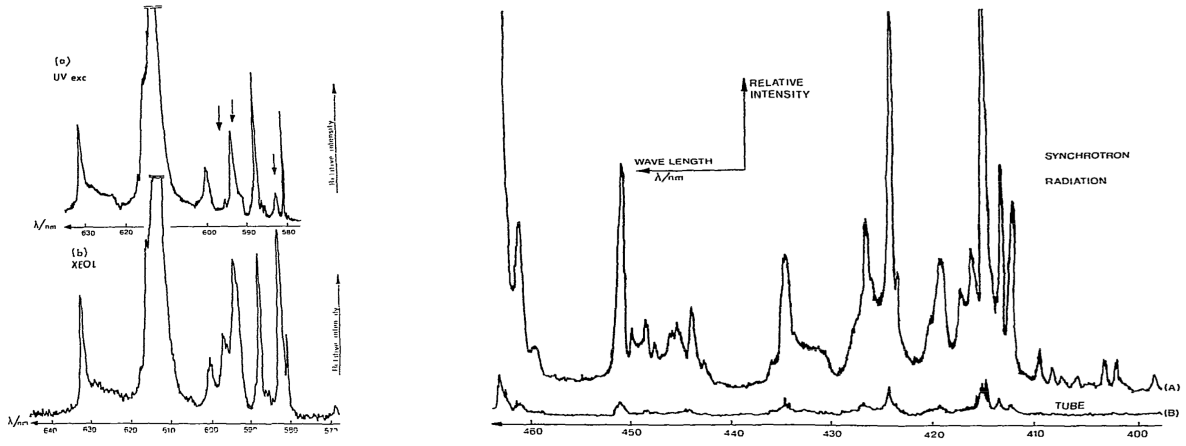

Figure 1.10: On the left, XEOL and UV excited Luminescence spectra from Y_2O_3 doped with Eu^{3+} obtained via UV and x-ray excitation, stacked for comparison. On the right, luminescence of Y_2O_3 obtained via x-ray excitation using a traditional x-ray tube (B) and a synchrotron radiation source (A); reprinted from [22] with permission.

opposed to the population by valence electrons [20, 21]. Contrasting the resonant absorption of traditional photoluminescence, the exited electron states provided via x-ray excitation have the potential to excite all available luminescence centers within a material. This allows a more comprehensive examination of the defect states within a material and utilizing XEOL in conjunction with our XAS and XES techniques, not only can the local environment of atoms be determined, but the associated defect states of those environments can be probed.

The usefulness of XEOL is best seen simply by graphical comparison. In Figure 1.10, the advantages of synchrotron-based XEOL measurements over traditional UV luminescence or x-ray tube-based XEOL measurements can be seen. Furthermore, experimental techniques can be further bolstered using a variety of calculation techniques, with the main focus for us being crystal field multiplet calculations.

1.6 Fundamentals of X-Ray Excitation

The initial, intermediate, and final states are described by the Hamiltonian, $\mathcal{H}$,

$$\mathcal{H} = \mathcal{H}_k + \mathcal{H}_{e/N} + \mathcal{H}_{e/e} + \mathcal{H}_{SO} + \mathcal{H}_{CF} \tag{1.3}$$

where $\mathcal{H}_k = \sum_i p_i^2/2m$ is the kinetic energy of N electrons with momentum p, and mass m, $\mathcal{H}_{e/N} = -\sum_i Ze^2/r_i$ is the electrostatic interaction of electron i with charge e with a nucleus at radius r_i with charge Z, $\mathcal{H}_{e/e} = \sum_j \sum_{i<j} e^2/r_{ij}$ is the electron-electron interaction with distance r_{ij} between two electrons i and j, $\mathcal{H}_{SO} = \sum_i \xi_i(r_i)(\mathbf{l}_i \cdot \mathbf{s}_i)$ with orbital and spin angular momentum operators $\mathbf{l}_i$, $\mathbf{s}_i$, and proportionality factor ξ_i, and $\mathcal{H}_{CF} = -eV(\mathbf{r})$ with a crystal field potential $V(\mathbf{r})$ further discussed below.

In classical density functional theory (DFT), the single particle approximation is used. In $3d$ transition metal compounds, significant contributions to the experimentally obtained XAS and RXES spectrum are from the $3d$–$3d$ and $2p$–$3d$ two particle interactions [23]. To calculate these explicitly, we need to consider atomic multiplets instead of the widespread DFT and use these in addition to a crystal field potential.

In the cluster model, we consider a transition metal with six oxygens surrounding it embedded in an electric field due to the charges of the other atoms and electrons of the crystal.

In addition to the close interactions of the cluster, we add the effect of the charges around the cluster via the Madelung potential resulting from all other atoms modeled as point charges around the cluster. This crystel field potential first encountered in Equation 1.3 can be defined as

$$V(r, \theta, \phi) = \sum_{k=0}^{\infty} \sum_{m=-k}^{k} A_{k,m} r^k C_k^m(\theta, \phi) \tag{1.4}$$

where $C_k^m(\theta, \phi) = \sqrt{\frac{4\pi}{2k+1}} Y_k^m(\theta, \phi)$, $Y_k^m(\theta, \phi)$ being the spherical harmonics.

The values of $A_{k,m}$ can be found using an Ewald summation over point charges using positioning from a given structure. This technique is referred to the "structure model" here. In addition to the structure model, we refer to the "parameterized model" for spectra, which

relies on an assumed crystal field splitting resulting from spatial positioning of the lattice. By assuming basic crystal structures (octahedral, tetrahedral, and distortions on each), $A_{k,m}$ parameters can be reduced in most cases from 15 to five, denoted $10Dq$, Ds, Dt, Du, Dv. The strength of this parameterized model is in the near guarantee of distinguishing between an octahedral and tetrahedral-like site. Since these are the most common structures within transition metal oxides, discerning between them often confirms the placement of an atom within a lattice versus an interstitial state. In addition to this, these five parameters can express distortion in the perfect coordinations often as a result of a non-typical ion being introduced into a crystal lattice.

In practicality, these methods are used in a bidirectional manner to reinforce the conclusions gained from one another. By first analyzing a system via the parameter model, the crystal field and therefore the coordination of an ion can be determined, giving a description of the positioning of the atom in a given material. Conversely, knowing the presence of distortions within the crystal field via the parameter model, the source of those distortions can be ascertained. Producing structures for specific distortions (eg. the presence of oxygen vacancies), the Madelung potentials resulting from each distinct structure can be generated and resulting spectra can be used to directly model proposed spectral changes.

Chapter 2

Indium Oxide

The first material we will investigate is In_2O_3, a WBGS with widespread integration in technology today. With studies already completed on DMS materials based on In_2O_3 using a variety of synthesis techniques and dopant atoms, completing a systematic study of the material using a single, widely applicable synthesis method and the $3d$ transition metals of interest allows a strong starting point for our spintronic investigation herein. The focus here is quite simple: the interaction of each dopant atom with the matrix of In_2O_3. Due to the inherent depth dependence of the ion implantation techniques discussed in Section 1.3, synchrotron-based x-ray techniques can be utilized to probe the materials both collecting the surface sensitive TEY, and the bulk sensitive PFY.

2.1 Contributions

It is important to note my role here as a synchrotron-based experimentalist. Sample synthesis is a complex and fascinating field, and many degrees have been completed specializing in this field alone. Instead of partaking in this aspect personally, I have the pleasure of being able to collaborate with groups around the world. This time, synthesis of the In_2O_3 thin films was completed by Dr. Brinzari of Moldova State University. The implantation of the cobalt, nickel, iron, and manganese was completed by Dr. Gavrilov of the Ural Branch of the Russian Academy of Sciences, and x-ray photoelectron spectroscopy (XPS) measurements were complete by Dr. Zhidkov, Dr. Kukharenko, and Dr. Kurmaev of the Ural Federal University. XPS measurements taken here are complimentary to the synchrotron-based methodologies completed by myself, Mr. Becker, and Dr. Leedahl from our research group in the Department of Physics to probe the bulk properties of the material and the total density of

states, where our techniques probe the partial density of states. In addition, Dr. Boukhvalov of Hanyang University was instrumental in interpreting the XPS results, comparing them to DFT calculations he performed. In addition to their inclusion in this manuscript, these results have also been submitted for publication in a peer-reviewed journal.

2.2 Introduction

Diluted magnetic semiconductors (DMS), in which the cations of a semiconductor material are partially substituted by the 3d transition metals, have attracted attention in recent years due to their potential applications in spintronics [24, 25, 26, 27]. 3d-doped wide band gap semiconductor oxides (ZnO and TiO_2) appear to be ideal candidates for such devices because of their potential to be produced consistently and in a controllable way. More recently, experimental reports have arisen on the room temperature ferromagnetism in 3d-doped In_2O_3, [28, 29, 30, 31, 32] which is known to be an n-type wide band gap transparent semiconductor. In_2O_3 has already been implemented in light-emitting diodes including flat-panel displays, solar cells, and a wide range of optoelectronic applications due to the high electrical conductivity, high optical transparency in the visible region, and high reflectivity in the infrared region. In_2O_3, with a variety of transition metal dopants, has been studied and promising ferromagnetic properties have been reported for a variety of synthesis techniques. [33, 34, 13, 35] However, investigations utilizing synchrotron-based techniques have primarily focused on single dopant atoms with varying synthesis techniques by x-ray absorption near edge structure (XANES) and extended x-ray absorption fine structure (EXAFS) techniques [36, 37]. Doping of In_2O_3 using 3d transition metal elements could integrate the optical and transport properties of In_2O_3 with the magnetic properties of the dopant within the same material, thus opening a unique opportunity to make a multi-functional device. A systematic investigation of the electronic structure and defect states under specific sample preparation conditions is crucial to drive this material forward to room temperature ferromagnetism and device applications.

Here, we have studied the electronic structure of In_2O_3 doped with Mn, Fe, Co, and Ni by employing x-ray photoelectron spectroscopy (XPS), x-ray absorption spectroscopy (XAS), and x-ray emission spectroscopy (XES). Experimental spectra obtained are compared to first-principles calculations of formation energies for different configurations of structural defects calculated using density functional theory (DFT) and to modeled spectra using crystal field multiplet calculations. By doing so, we can give a comprehensive picture of the electronic structure, disordering effects, and the substitution mechanisms within the material.

2.3 Experimental and Calculation Details

The samples were prepared using the spray pyrolysis method to deposit the In_2O_3 film on polished 1 × 1 cm^2 silicon substrates. A 0.2 M water solution of $InCl_3$ was deposited at a pyrolysis temperature of 450°C, forming a ∼100 nm In_2O_3 layer. The uniformity of the deposited film was improved by synchronous rotation of the sample holder and the nozzle swing along with the $InCl_3$ solution being sprayed perpendicular to the sample holder. The solution was applied in several cycles, each lasting no more than 30 seconds (sprayed solution volume did not exceed 1.5 ml), maintaining a temperature between 440-460°C during the deposition process and provided an average film growth rate of 1-2 nm/s. Such conditions provide the growth of nanoscale grains with an average size of ≈20 nm, which have a cubic crystalline structure that belongs to the $Ia\,3$ space group (bixbyite) [38, 39]. A lattice constant of 1.0118 nm was obtained for the In_2O_3 samples using x-ray diffraction and the average roughness of the films was no more than 5 nm with preferential texturing along the [400] direction. Lastly, the effective porosity of the In_2O_3 was estimated to be 20% using refractive index measurements.

Mn, Fe, Co, and Ni were implanted in the In_2O_3 thin films using a metal-vapor vacuum arc ion source. The operating pressure in the implantation chamber did not exceed 2.0 × 10^{-2} Pa. The ion beam energy was set to 30 keV by vapourizing the metal with an electric arc at the cathode and the pulse duration was 0.4 ms with a current density of 0.6 mA/cm^2 which gave an ion fluence (flux integrated over time) of 2 × 10^{17} cm^{-2}. A defocusing of the ion beam was applied in order to achieve a lateral uniformity of implanted ions within the host material.

X-ray photoelectron spectroscopy (XPS) measurements were made by using a PHI XPS Versaprobe 5000 spectrometer with a quartz monochromator. The XPS energy analyzer was supporting the working range of binding energies from 0 to 1500 eV with an energy resolution of $\Delta E \leq 0.5$ eV for Al $K\alpha$ radiation (1486.6 eV). As in our previous studies, the samples were held in a vacuum (10^{-7} Pa) for 24 hours prior to measurement, and only samples whose surfaces were free from micro impurities (as determined by means of surface chemical state mapping) were measured and reported herein. XPS spectra were recorded under monochro-

matized Al $K\alpha$ X-ray emission with a spot size of 100 μm. An x-ray power load delivered to the sample did not exceed 25 W in order to avoid x-ray stimulated decomposition of the sample. Under these conditions an XPS signal-to-noise ratio of 10000:3 was achieved. Primarily, the spectra were processed using ULVAC-PHI MultiPak Software 9.3.

The x-ray absorption spectroscopy (XAS) measurements were taken on the REIXS and SGM beamlines at the Canadian Light Source, with a resolving power E/ΔE=5000 using an energy resolved silicon drift detector for partial florescence yield (PFY) detection [40, 41]. X-ray emission spectroscopy (XES) measurements were taken on Beamline 8.0.1 at the Advanced Light Source with a resolving power of 2000 [42].

Density-functional theory (DFT) based modeling was performed using the SIESTA pseudopotential code [43]. All calculations had been made employing the Perdew-Burke-Ernzerhof variant of the generalized gradient approximation (GGA-PBE) [44] for the exchange-correlation potential. The ground electronic state was consistently found during optimization using norm-conserving pseudopotentials [45] for the cores and a double-ξ plus polarization basis of localized orbitals. Full optimization of lattice constants and atomic positions were performed. The forces and total energies were optimized with an accuracy of 0.04 eV/Å and 1.0 meV, respectively. All calculations were carried out with an energy mesh cut-off of 300 Ry and a k-point mesh of 6×6×6 in the Monkhorst-Pack scheme [46]. In order to plot the final densities of states (DOS), the k-point mesh was increased to 8×8×8.

The crystal field multiplet calculations use the approach originally formulated by Cowan [47]. The Quanty full multiplet software was utilized, taking both 2p-3d and 3d-3d transitions into account via Slater integrals calculated in the Hartree-Fock approximation [48]. The crystal field multiplet calculations are used in two metholologies: the first yields parameters ($10Dq$, Ds, Dt) relating to the energy level splitting of the 3d valence orbitals. In addition, an artificial scaling parameter of the Slater integrals, β, is introduced to account for many-electron correlation effects not taken into account in the Hartree-Fock approximation. The second uses an atomic structure of the host crystal lattice (In_2O_3 in this case) and calculates the Madelung potential of the structure using an Ewald summation over point charges [49]. By combining these two approaches, referred to here as the "crystal field model" and "structure model" respectively, allows the bidirectional connection of the

experimentally measured spectra with modeling, and not only investigates the positioning and local structure of dopants, but the mechanisms behind any distortions observed.

2.3.1 XPS Measurements

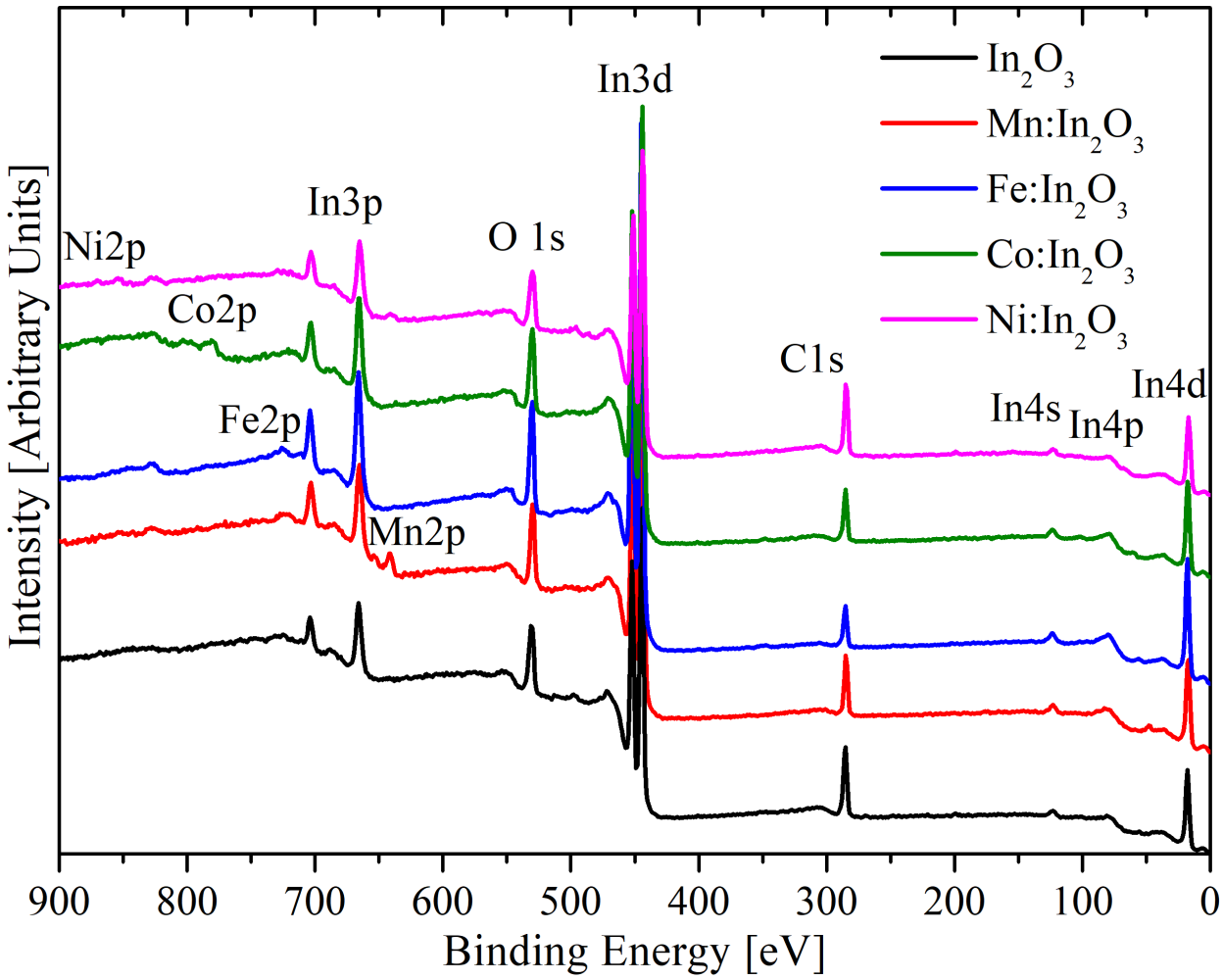

Figure 2.1: XPS survey spectra of doped In_2O_3 reveal low carbon content within the samples under investigation.

The XPS survey spectra measured at the binding energy range of 0-900 eV are presented in Figure 2.1. The XPS spectra were calibrated using the carbon 1*s* core energy level of 285.0 eV as the reference energy. The XPS measurements of core levels in doped In_2O_3 thin films are presented in Fig. 2.2.

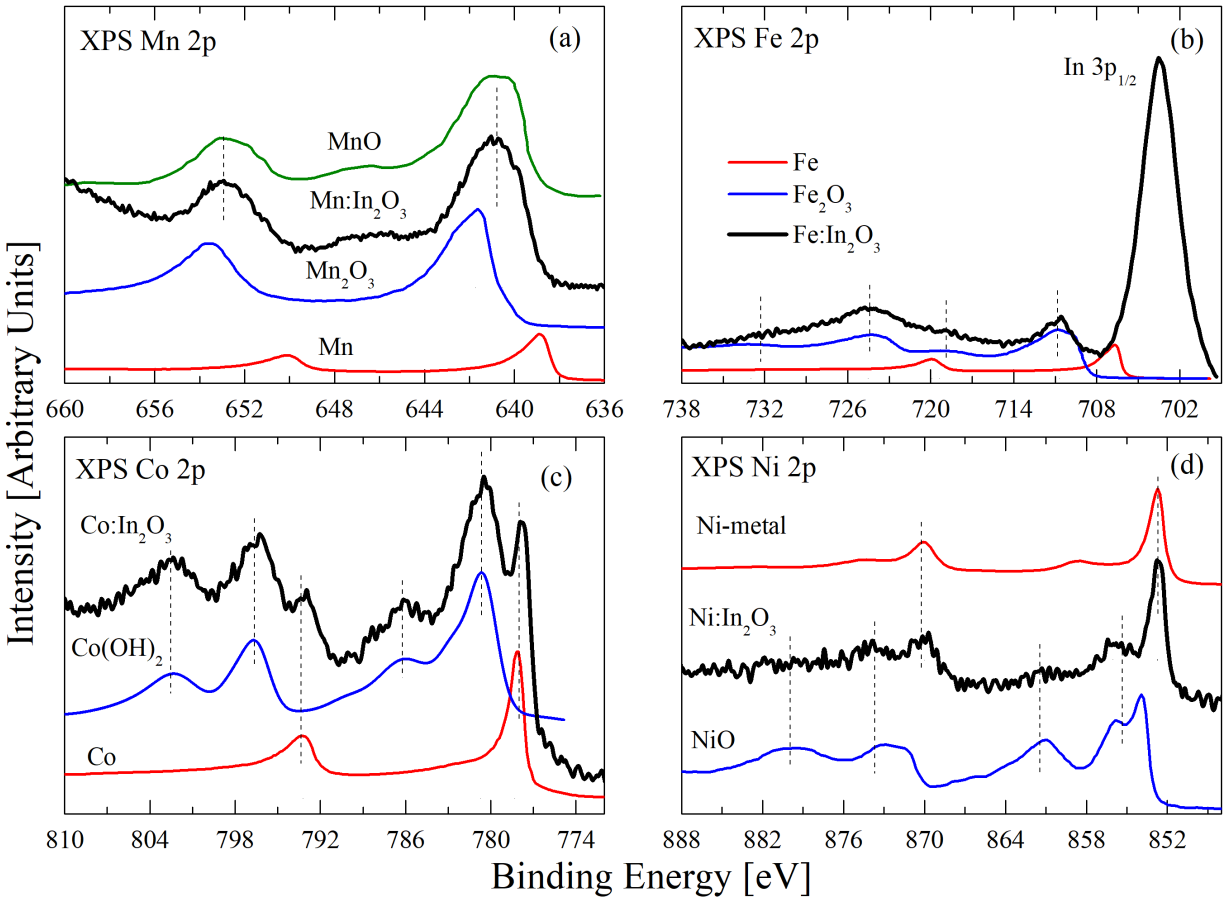

Figure 2.2: XPS spectra of Mn, Fe, Co, and Ni dopants in in In_2O_3. (a) Mn dopant in In_2O_3 primarily shows Mn^{2+}. (b) Fe dopant in In_2O_3 primarily shows Fe^{3+}. (c) A combination of $Co^{2+}$and clustering of Co atoms can be seen in XPS spectra of Co doped In_2O_3. (d) A combination of Ni^{2+} and clustering of Ni atoms can be seen in XPS spectra of Ni doped In_2O_3.

The comparison of metal XPS 2p spectra of Mn:In_2O_3 and Fe:In_2O_3 with spectra of reference samples show that in these systems, the cation substitution takes place without any traces of clustering metal atoms. On the other hand, in the spectra of Co:In_2O_3 and Ni:In_2O_3, additional signals are found at energy positions which coincide with those of pure metals. This indicates both cation substitution and clustering of impurity atoms are present in these systems. XPS valence band spectra (Fig. 2.3) are found to be in full agreement with measurements of metal XPS 2p spectra (Fig. 2.2). One can see that XPS valence bands of Mn:In_2O_3 and Fe:In_2O_3 are very similar to those of undoped In_2O_3 whereas in the spectra of Co:In_2O_3 and Ni:In_2O_3 additional high-energy sub-bands are those that can be attributed

to the formation of metallic states.

2.3.2 Calculations

In_2O_3 supercells consisting of 80 atoms were used as the host for our calculations (Fig. 2.4). Based on previous theoretical investigations [50], substitutional (S), interstitial (I) and their combination of (xS+I) type transition-metal impurities were also considered. In addition, the influence of possible oxygen vacancies via the inclusion of a single oxygen vacancy (vO) was modeled. The calculations of the formation energies (E_{form}) were based on the following formula:

$$E_{\mathrm{form}} = \frac{E_{\mathrm{total}} - (E_{\mathrm{matrix}} - \mathrm{n}E_{\mathrm{removed}} + \mathrm{m}E_{\mathrm{added}})}{\mathrm{m}} \tag{2.1}$$

where $\mathrm{E_{total}}$ is the total energy of the system with the current configuration of defects, $\mathrm{E_{matrix}}$ is the total energy of the system (with or without oxygen vacancies) before formation of the studied configuration of defects, $\mathrm{E_{removed}}$ and $\mathrm{E_{added}}$ are the total energies in the ground state of the pure materials (indium or transition metal), n and m are the number of removed and added atoms, respectively.

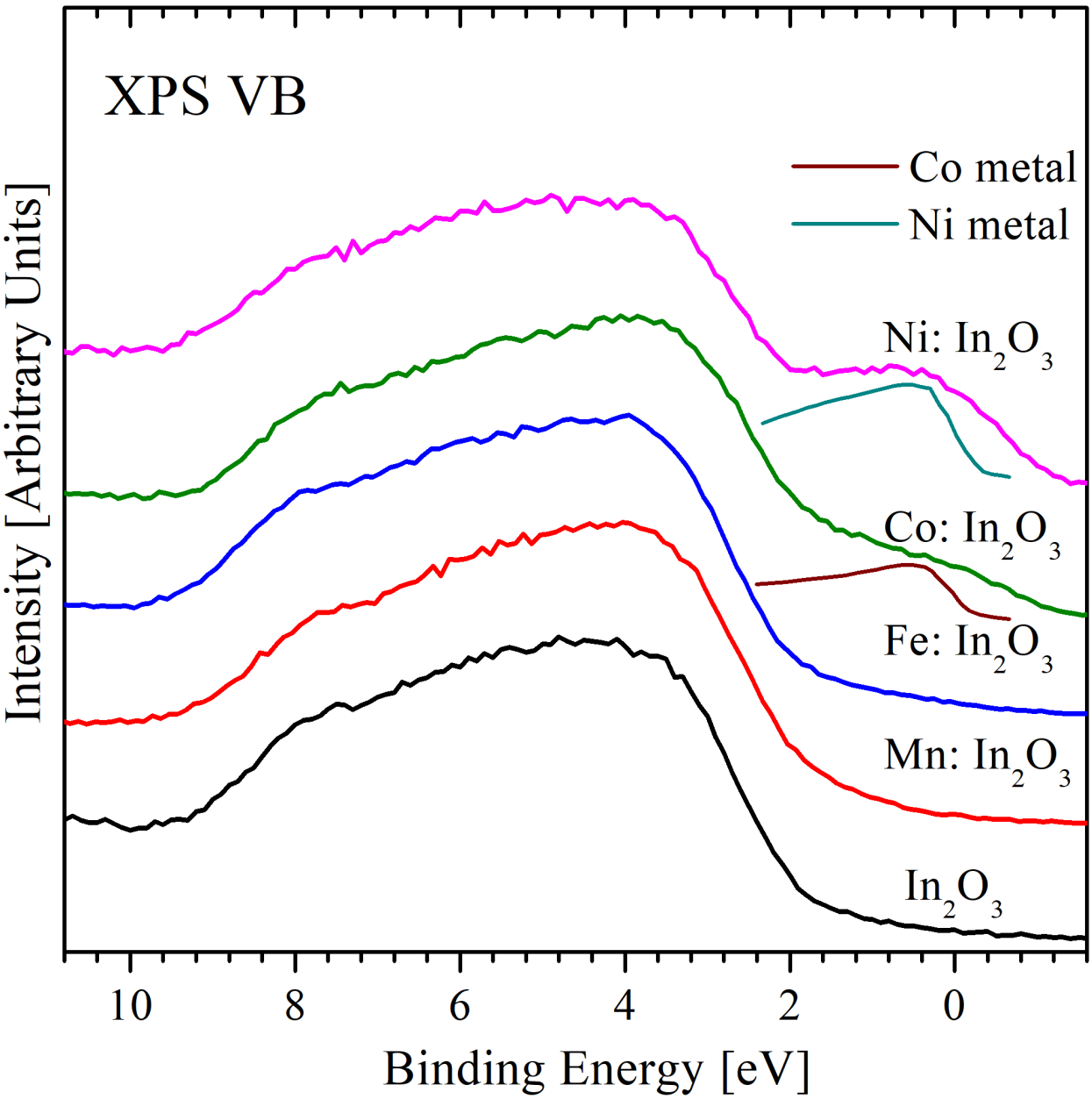

Figure 2.3: XPS valence band spectra of Mn, Fe, Co, and Ni doped In_2O_3. The low energy metallic signals are highlighted in Ni:In_2O_3 and Co:In_2O_3 by the display of pure metal spectra.

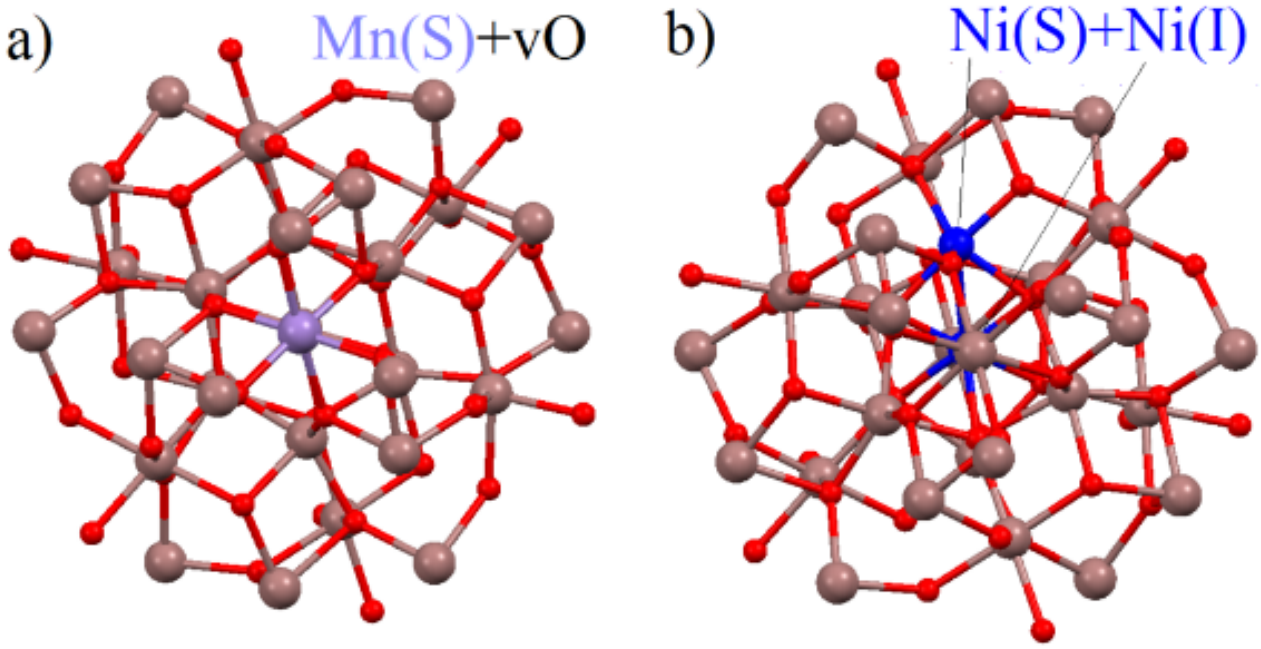

Figure 2.4: Optimized atomic structures of two different configurations of substitutional (S), interstitial (I) 3d-impurities and oxygen vacancies (vO) in In_2O_3 supercell.

Table 2.1: Formation energies (eV/impurity) for various configurations of substitutional (S) and interstitial (I) impurities. In parenthesis, the formation energies for the same configurations in vicinity of single oxygen vacancy (vO) are reported. The energies corresponding to the most probable defects are marked in bold.

	$Mn:In_2O_3$	$Fe:In_2O_3$	$Co:In_2O_3$	$Ni:In_2O_3$
S	-1.08 (**-1.84**)	**+0.64** (**+0.53**)	+0.38 (+0.50)	+1.51 (+0.80)
2S	-1.18 (**-1.76**)	+**0.76** (**+0.72**)	**+0.27** (**+0.29**)	+1.44 (+0.77)
S+I	**-1.80** (-1.37)	+0.81 (+1.02)	**+0.19** (+0.41)	**+0.48** (+0.81)
2S+I	-1.67 (-1.66)	+0.80 (+0.83)	+**0.24** (**+0.23**)	+**0.71** (**+0.65**)

From the calculation (Table 2.1), it can be seen that only iron has a stable tendency to form substitutional defects. This is due to the fact that the most common iron oxide (Fe_2O_3) has a similar atomic structure to the host In_2O_3. The presence of oxygen vacancies only slightly reduces the energy required for the formation of substitution defects. This result agrees qualitatively with the results of the XPS measurements, where the spectra of iron impurities are practically identical to the spectra of Fe_2O_3. The presence of iron defects both in the absence and in the presence of oxygen vacancies leads to the disappearance of the energy gap (Fig. 2.5b), but there is no significant contribution to the electronic structure near the Fermi level, which qualitatively coincides with the experiment.

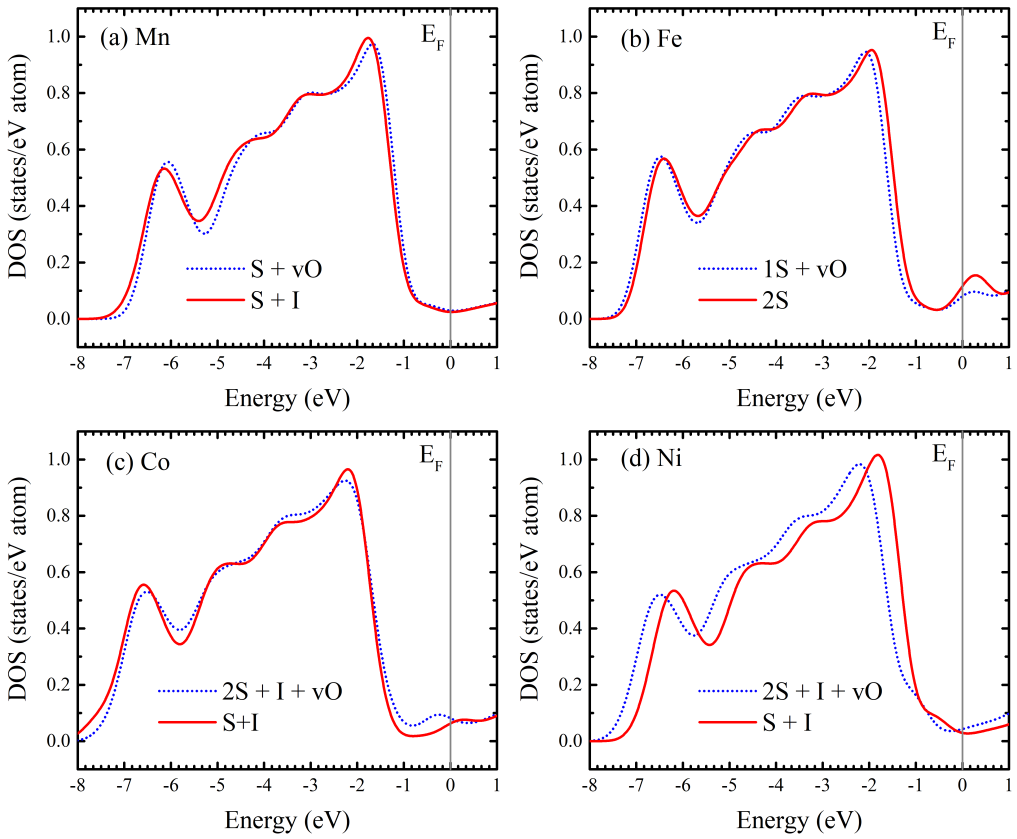

Figure 2.5: Total densities of states for the most probable configurations of substitutional (S) and interstitial (I) impurities (see discussion in the text) with (dashed blue line) and without (solid red line) oxygen vacancies (vO).

In the case of manganese impurities in the absence of oxygen vacancies, the pairs of substitution and interstitial defects (S + I) are formed which, however, does not lead to a significant change in the electronic structure (Fig. 2.5a). This is due to the difference in the ionic radii of indium and manganese, and the ability of manganese to form various oxides of Mn_xO_y. The presence of oxygen vacancies creates local distortions of the crystal lattice of In_2O_3, which reduces the effect of the difference in the ionic radii and increases the probability of substitution defects forming. These vacancies also do not lead to a visible change in the electronic structure of the valence band (Fig. 2.5a). This result explains qualitatively why, in contrast to iron impurities, the XPS spectra of the manganese impurities contain a combination of both the spectra of Mn_2O_3 and MnO. Formation energies of substitutional and interstitial defects for cobalt and nickel are close. This is due to the fact that the most widespread oxidation state for Co is 2+, and not 3+ found with indium in the host

material. The presence of oxygen defects does not significantly change the energy of various configurations. The formation of such configurations, both in the absence and in the presence of oxygen vacancies, leads to the appearance of an additional contribution to the DOS just before the Fermi level (Fig. 2.5c, d), which coincides with the experimental spectra of the valence band.

2.3.3 X-Ray Absorption and Emission

Manganese. The presence of the XAS energy feature at 641eV denotes the majority presence of Mn^{2+} comparing to the reference spectra of MnO, confirming the results found using XPS. From the crystal field model with a $10Dq$ value of 0.2 eV and a Slater integral scaling of 0.71, while some Mn^{2+} ions may be found in substitutional locations, the majority of ions will be placed in an Mn^{2+} interstitial positioning within the material.

The interactions of the dopant are modeled via an effective potential, describing the bonding states within the local environment. By generating this effective potential using the host crystal structure and scaling the magnitude of this effective potential, the structural model in Figure 2.6 is generated. In this scenario, the 20% scaling of the effective potential signifies the low interaction of the Mn^{2+} ions with the host lattice, once again suggesting a low probability of substitution and a high likelihood of interstitial states. The increased spectral weight of the feature at $\approx$ 642eV can be attributed to small amounts of Mn^{3+} as displayed in the XPS data, which is observed equally in the TEY and PFY spectra, indicating that the incorporation of Mn ions does not differ on the surface in comparison to the bulk.

Cobalt. Comparing to CoO and Co-metal reference spectra, cobalt dopants within In_2O_3 show many similarities to cobalt metal spectra using XAS. Examining the crystal field model with a $10Dq$ value of -0.4 eV, a Ds value of -0.15 eV and a Slater integral scaling of 0.65, the tetrahedral coordination of the cobalt with significant distortion (represented by the Ds value) demonstrates the interstitial states that are present since this is contrary to the octahedral structure of In_2O_3. The agreement with a structure model signifies that substitutional states are possible, but with low probability, further supported by spectral agreement with cobalt metal reference spectra. With high similarity of PFY to TEY spectra, this leads to the conclusion of low substitutional states and significant interstitial and clustering states

present with no discernable difference between the surface and the bulk.

Nickel. Nickel implanted within In_2O_3 when compared to NiO and Ni-metal spectra in Figure 2.8 show high similarities metallic nickel in surface states, indicated by the TEY spectra, and the increased weight of peak at 855 eV seen in the PFY spectra indicates the difference in interaction within the material at the surface differing from the bulk. Comparing the ratio in peak intensities $I(L_2)/I(L_3)$ of the resonant excitation at the L_2 edge in Ni-metal, this confirms the majority contribution of metallic nickel to the spectra in the bulk [51]. Therefore, it can be concluded that while substitutional states are present, they are the minority interaction in the material.

Iron. Examining iron XAS spectra in Figure 2.9, we see strong similarities to Fe_2O_3. Crystal field parameters of $10Dq = 2.4$, $Ds = -0.10$ and $Dt = 0.15$ with a Slater integral scaling of 0.65 for Fe^{3+} suggest an octahedral coordination, corresponding to a stable tendency to form substitution defects for these ions. In addition, good agreement of the PFY spectra to a substitutional model with an oxygen vacancy adjacent to the iron site, follows the oxygen vacancy results found for pulsed laser deposition grown iron doped In_2O_3 [13]. Here, spectral weight differences in the PFY and TEY spectra can be attributed to instrumentation and the probability of Fe^{2+} states below the sensitivity of our modeling.

2.4 Conclusion

We have performed a systematic study on the dopant atoms within In_2O_3, which provides key insight into a leading material for DMS systems. Through investigation of Mn, Fe, Co, and Ni within the host In_2O_3, we show the influence of 3d transition metals on the crystal lattice with subsequent distortions and impurity states, noting the sharp differences with each dopant atom. This contrast can be clearly seen in the investigation of oxygen vacancies and varying success of substitution seen in the samples, provided by a direct link between experimental results and molecular geometry. By building on the investigation of ion implanted techniques the strong effect of synthesis methodology on the properties of DMS systems can be investigated through further work on In_2O_3 and other metal oxides to bring this promising area of materials research into new technologies.

2.5 Acknowledgements

The work in this chapter was supported by the Natural Sciences and Engineering Research Council of Canada (NSERC), the Canada Research Chairs program. Research was enabled in part by computing resources from Westgrid and Compute Canada. XAS measurements were performed at the Canadian Light Source which is supported by the Canada Foundation for Innovation, Natural Sciences and Engineering Research Council of Canada, the University of Saskatchewan, the Government of Saskatchewan, Western Economic Diversification Canada, the National Research Council Canada, and the Canadian Institutes of Health Research. XES measurements were performed at the Advanced Light Source, which is a DOE Office of Science User Facility under contract no. DE-AC02-05CH11231. XPS measurements were supported by RFBR (Project 17-08-00395), grant program of the President of Russian Federation (Grant No. MK-1145.2017.2), the Government of Russian Federation (Act 211, Agreement No. 02.A03.21.0006), and the Russian Federal Agency of Science Organizations (Project "Electron" No. AAAA-A18-118020190098-5).

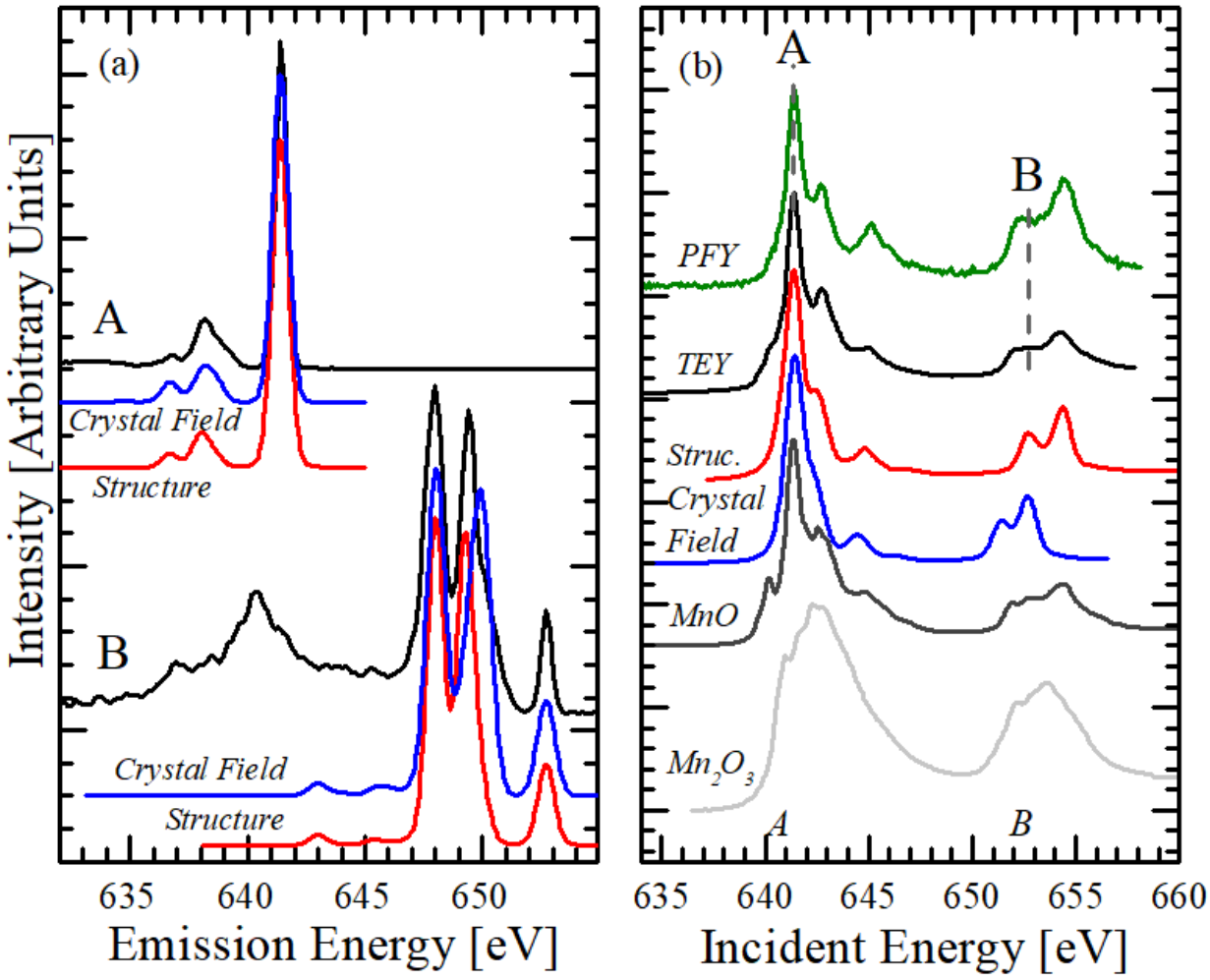

Figure 2.6: XAS and XES spectra of Mn implanted in In_2O_3. Grey XAS spectra display MnO and Mn_2O_3 standard references for comparison. Spectra calculated using crystal field parameters (blue) and using a substitutional ion within a host lattice structure (red) are displayed. Due to a reported $10Dq$ value of 0.2 eV and a low interaction indicated by a 20% scaling of the crystal field potential, interstitial Mn^{2+} is shown to be the highest likelihood valence.

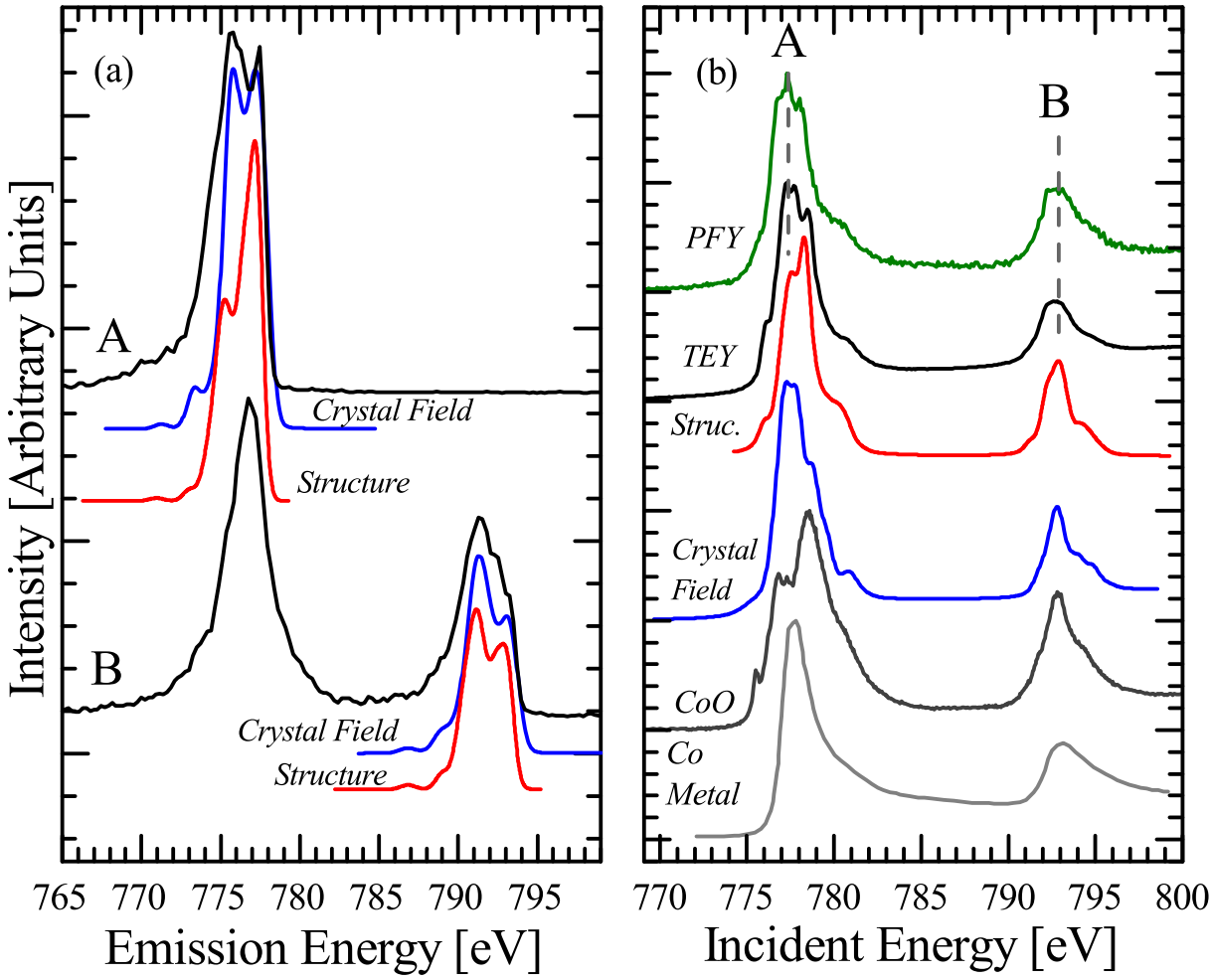

Figure 2.7: XAS and XES Spectra of Co implanted in In_2O_3. In Fig. 2.7(b), Co-metal and CoO standard references are displayed (grey) for comparison. Matching measured TEY and PFY (black and green) to calculated spectra both using a structural model (red) and a parameterized crystal field model (blue) demonstrates the low likelihood of substitution and the presence of interstitial and clustering states.

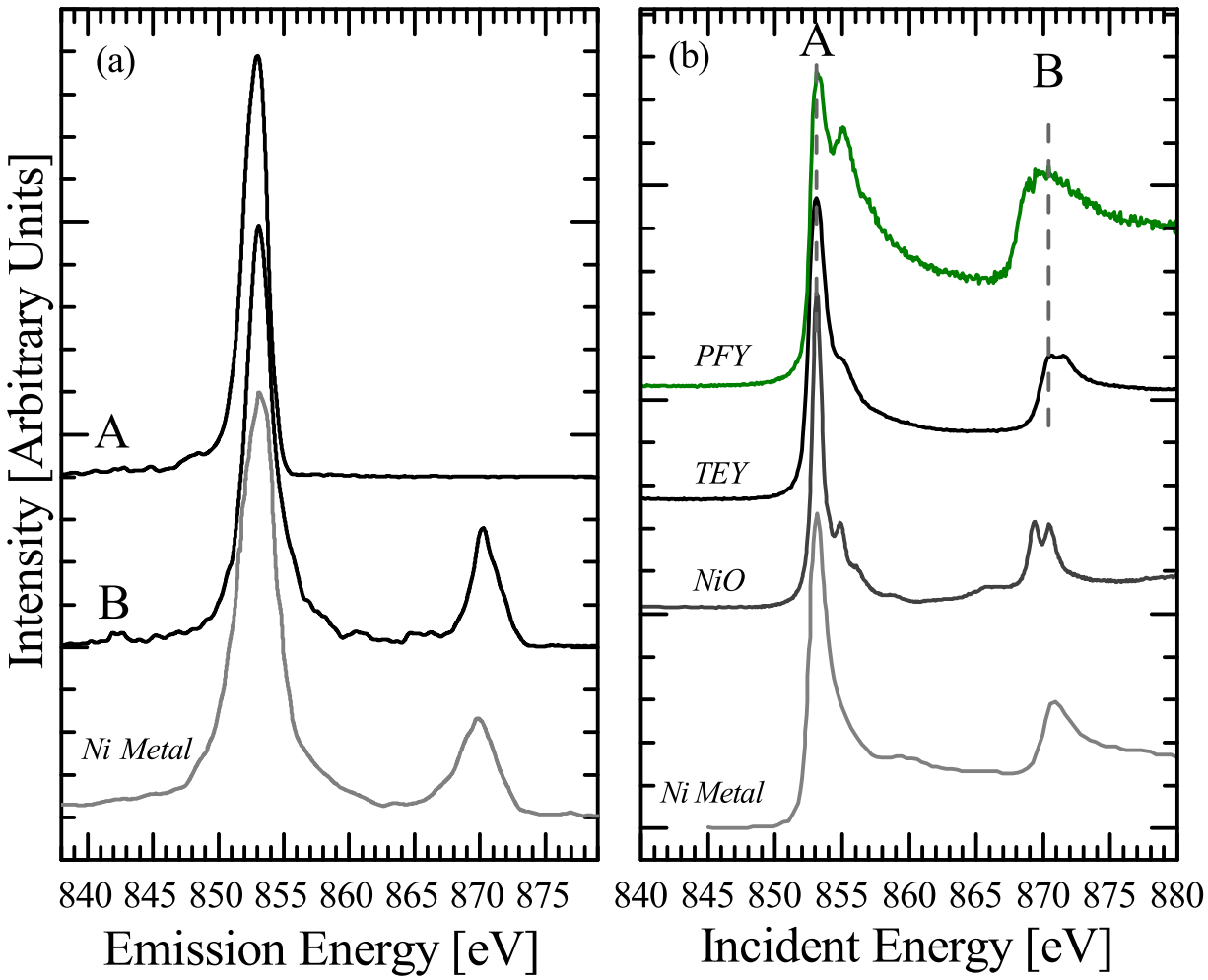

Figure 2.8: XAS, XES Spectra of Ni implanted in In_2O_3. A Ni-metal reference is included in (a) for XES and reference spectra for NiO and Ni-metal are included in (b) for XAS (grey). The TEY measurement (black) indicates the majority metallic clustering states occurring at the surface and the additional peak at 855 eV in the PFY measurement (green) indicates the presence of substitution states in the bulk.

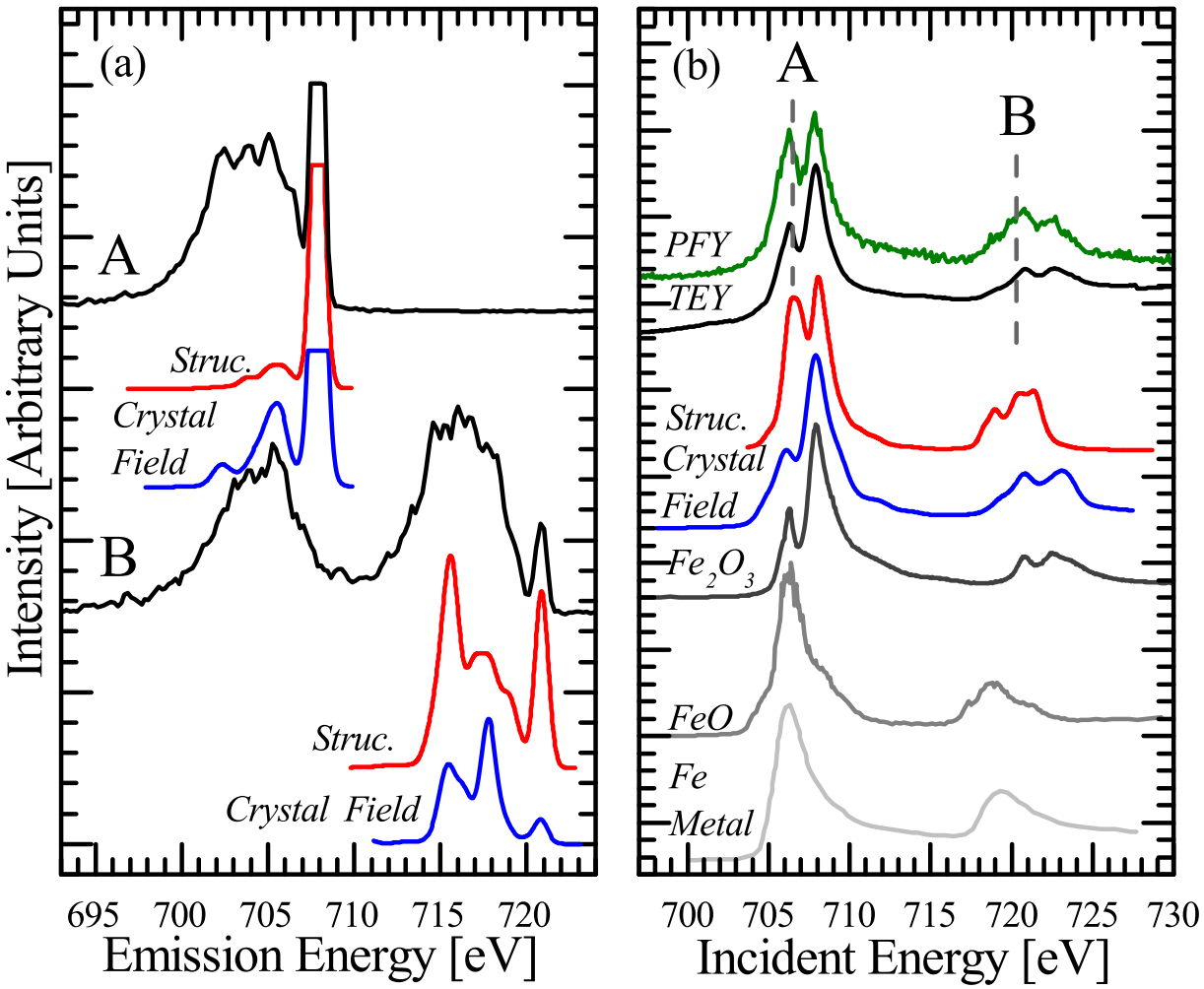

Figure 2.9: XAS and XES Spectra of Fe implanted in In_2O_3. Spectra simulated using crystal field models in blue and red are shown, demonstrating the substitution of iron in a 3+ valence state into the host In_2O_2. The red spectra displayed includes an oxygen vacancy adjacent to the substitutional iron site. This simulation of spectra inclusive of oxygen vacancies confirms their role in the distortions displayed in extracted crystal field parameters.

Chapter 3

Tin Oxide

Our studies of In_2O_3 allow us to understand the effects of a single synthesis method on substitution and defect properties of a DMS system. Next, we investigate a more complicated case: SnO_2 is again a wide band gap semiconductor but dissimilar to our work with indium oxide, we investigate the effects of an important preparation technique: annealing. The heating of samples to high temperatures (in our case $\sim 800°C$) can bring important chemical and structural changes to a material after initial synthesis. This is often used in "wet synthesis" methods like the hydrothermal method described herein. Through this, and by investigating differing concentrations of a novel co-doped DMS system, we can gain key insight on the effects of annealing and yet-unseen detail on oxygen vacancies – one of the defects investigated in the prior study of indium oxide.

3.1 Contributions

Similar to the indium oxide samples, all sample synthesis and magnetic characterization was performed by collaborators, this time at Pondicherry University in Puducherry, India. Without the expertise of Dr. R. Murugan and Dr. D. Manikandan, these results would not have been possible. In addition to this, the work of my colleagues Dr. Brett Leedahl in mentorship during this project both in modelling and experimental measurements as well as Mr. Tristan de Boer with DFT modelling. In addition to their inclusion in this manuscript, these results have also been submitted to a peer-reviewed journal.

Spin electronics, or *spintronics* relies on detecting and manipulating electron spin in addition to electron charge. The movement of spin, like the flow of electron charge, could be used to convey information, creating devices that are smaller and consume less electricity than current solutions. One attractive candidate for spintronic materials are dilute magnetic semiconductors (DMSs), where transition metal (TM) impurities are introduced into a semiconductor host lattice to induce magnetic properties in an otherwise non-magnetic semiconductor. For real-world spintronic devices, a DMS must demonstrate ferromagnetic properties far above room temperature.

Tin Oxide (SnO_2) has garnered a significant amount of interest in these applications as a semiconductor with a large band gap ($\sim$ 3.6 eV), relatively low cost, and nontoxicity. Some studies on TM-doped tin oxide have been performed and room temperature ferromagnetism (RTFM) has been reported with various dopants both ferromagnetic and non-ferromagnetic [52, 53]. To move forward with this promising material, it is crucial to understand the effect of various dopants on the host material. Experiments suggest that the RTFM in TM-doped SnO_2 is related to oxygen vacancies, possibly due to trapped electrons within the host lattice [54]. Past investigations of doped SnO_2 reveal that at higher concentrations of dopants, materials can lose their magnetic properties, possibly due to a disordering caused by dopants on the host structure, or dopant clustering [55].

Synchrotron-based techniques have been used to investigate TM-doped SnO_2 with both ferromagnetic and non-ferromagnetic dopants (Zn, Co, Cr, Fe, Ni) including co-doped iron and nickel primarily using x-ray absorption near-edge structure (XANES) and extended x-ray absorption fine structure (EXAFS) techniques [56, 57, 58, 59]. In samples with zinc, cobalt, iron, and nickel dopants, oxygen vacancies are reported adjacent to substitutional dopant sites which compensate for the charge difference between dopants and the displaced Sn^{4+}. In the case of chromium substitution, Cr^{4+} ions cause a decrease in inherent oxygen vacancies in nanoscale SnO_2.

Investigations of cobalt doped SnO_2 and zinc doped SnO_2 show that both materials lose their ferromagnetic properties at low concentrations ($\sim$ 3%). Co-doping can in general be efficient for increasing the dopant solubility, lowering the ionization energy of acceptors and donors, and increasing carrier mobility so it is useful to investigate this material to fully

understand the effect of dopant concentration on the final material properties [60]. Here we will examine SnO_2 nanoparticles co-doped with varying concentrations of both zinc and cobalt to investigate distortions to the SnO_2 lattice due to the introduction of two dissimilar dopants. We present direct evidence for successful incorporation of dopants into a host SnO_2 material via x-ray absorption spectroscopy (XAS), x-ray emission spectroscopy (XES), and x-ray excited optical luminescence (XEOL) measurements. Furthermore, via crystal field modeling we link this luminescence with the oxygen vacancies adjacent to dopant sites and attribute distinct luminescence parameters to specific dopants within the material, allowing a rigorous and complete picture on the mechanisms of co-doping and annealing for the synthesis of spintronic materials.

3.2 Experiment and Theory

Undoped SnO_2, $Sn_{0.95}Co_{0.025}Zn_{0.025}O_2$, $Sn_{0.925}Co_{0.05}Zn_{0.025}O_2$, $Sn_{0.925}Co_{0.025}Zn_{0.05}O_2$, $Sn_{0.90}Co_{0.05}Zn_{0.05}O_2$, and $Sn_{0.85}Co_{0.075}Zn_{0.075}O_2$ were prepared by the hydrothermal method; detailed information regarding the synthesis of these materials can be found in a previous publication [61]. In addition to the drying process for all of the samples, a set was also annealed at 800°C for two hours in an air atmosphere. These are referred to as the "annealed" samples herein, compared to the "as-synthesized" samples. RTFM has been reported by Manikandan et al. for this system, however the mechanism is still unknown [61].

The XES and XAS measurements probe the partial occupied and unoccupied density of states of a material, respectively. XES records the emission resulting from decay from occupied states to fill core holes and the XAS monitors the excitation of core electrons into previously unoccupied states. XAS measurements were taken on the REIXS beamline at the Canadian Light Source (CLS), with a resolving power $E/\Delta E = 5000$; this was completed using a silicon drift detector for partial florescence yield detection. XES measurements for cobalt were taken on Beamline 8.0.1 at the Advanced Light Source, and for oxygen on the REIXS beamline at CLS with a resolving power of 2000.

The physical and electronic structure of defected and pristine SnO_2 was modeled using density functional theory with WIEN2k, a full-potential, all electron code, which uses

linearized augmented plane waves in a Kohn-Sham scheme [62]. The PBEsol exchange-correlation functional, a generalized gradient approximation functional formulated to optimize the properties of densely packed solids was used to perform the calculations [63]. An $RK_{max} = 7.0$ was used with a k-mesh selected so that the total energy was stable to within 10^{-5} Ry. This resulted in a k-mesh of $10 \times 10 \times 14$ for the unit cell of SnO_2. The lattice parameters for SnO_2 are based on the neutron diffraction determined lattice [64]. For calculations involving dopants and vacancies, these defects were added to a $2 \times 2 \times 2$ SnO_2 supercell, with a correspondingly smaller k-mesh. The DFT calculations are also used to calculate the electronic band structure as well as the Zn L-edge XAS spectra, allowing for a detailed comparison with experiment. These spectra are calculated by multiplying the partial density of states with a dipole transition matrix and radial transition probability [65]. All of the band structure diagrams are shown for a path in the Brillouin zone for the single unit cell of SnO_2 [66]. For supercell calculations, points in the supercell Brillouin zone have been mapped to the original unit cell representation using a Bloch spectral density approach as described in [67].

Due to the strong electron hybridization effects of the $3d$ electrons, cobalt spectra are modeled more accurately by considering multiplet effects [68]. The Co $L_{2,3}$ XES and XAS spectra are modeled using crystal field multiplet calculations in the approach originally formulated by Cowan [47]. The Quanty full multiplet code was utilized in two methodologies [48]. Firstly, crystal field parameters resulting from d orbital energy splitting can be used to describe the local coordination of the Co atoms and understand the overall lattice structure of the molecule, matching results from experiment. Secondly, supercells obtained through relaxing structures with implanted dopants via DFT can be used to generate the Madelung potentials of the crystal structure using an Ewald summation over point charges [49] and the subsequent potentials used to model the spectra via the same multiplet-based crystal field calculations.

3.3 Results and Discussion

3.3.1 Co L-edge

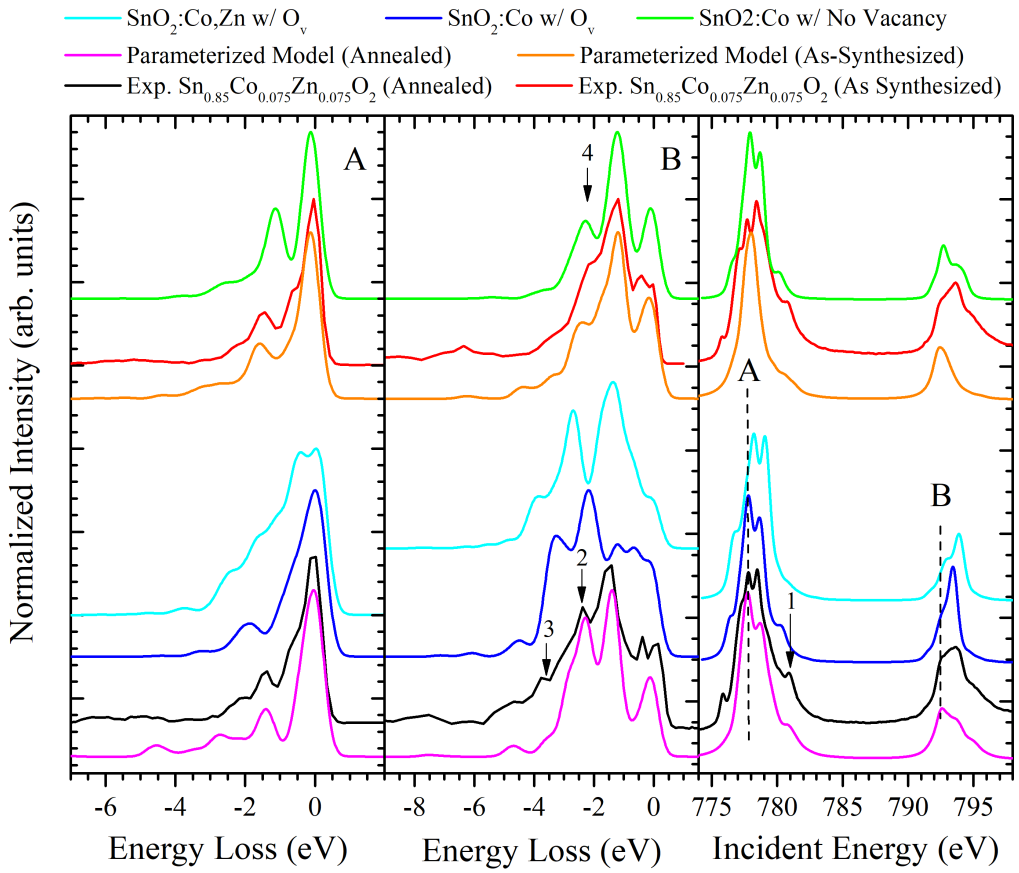

Figure 3.1: Comparison of experimental XAS and XES spectra to calculations. A parameterized model indicates a distorted tetrahedral coordination, where both the structural models indicate agreement between a Co with O vacancy model for the as-synthesized case, and a Co/Zn with O vacancy for the annealed case.

The Co L-edge emission and absorption spectra are shown in Figure 3.1. The L-edge allows the investigation of the excitations from the $2p$ orbitals to the unoccupied conduction band states. In addition the decay and subsequent emission allow insight into the d–d transitions and charge transfer excitations resulting from reordering of electrons within the $3d$ orbitals and lattice interactions. Through crystal field modeling, crystal field splitting values of $10Dq = -1.6$, $Ds = -0.1$, $Dt = -0.2$, and Slater integral scaling of 70% of their Hartree-Fock values (an artificial reduction of the intra-atomic electron-electron interactions) indicate

a distorted tetrahedral environment surrounding the Co atoms. This result agrees with the substitution of Co^{2+} into the Sn^{4+} sites since rutile SnO_2 has a space group of $P4_2/mnm$. Similar parameters can be seen for the as-synthesized $Sn_{0.85}Co_{0.075}Zn_{0.075}O_2$ (Figure A.1) indicating a warped tetrahedral coordination with $10Dq = -0.5$, $Ds = -0.2$, $Dt = -0.2$, and a Slater integral scaling of 55%.

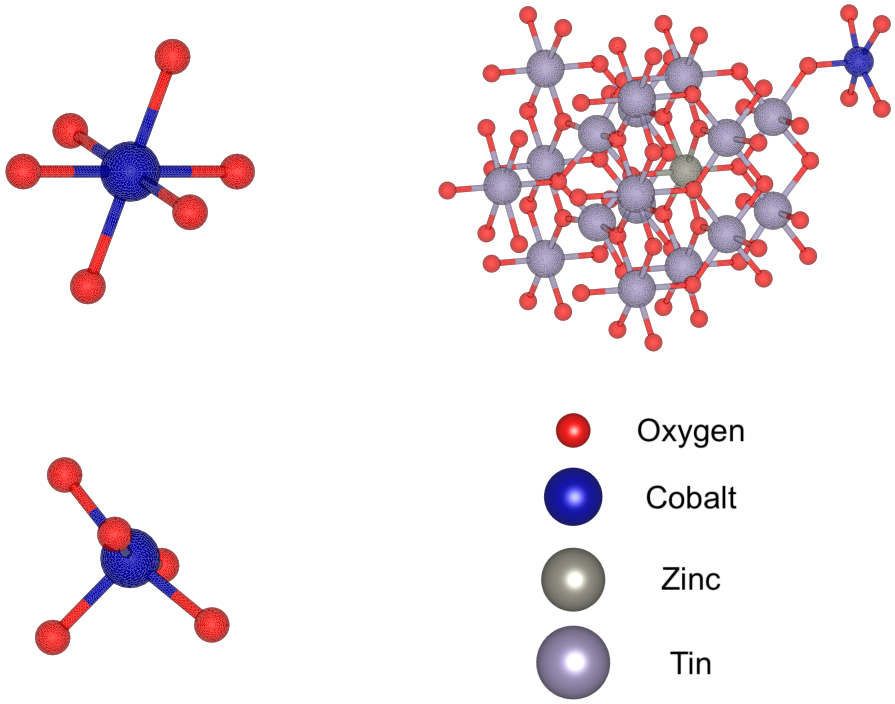

Figure 3.2: Relaxed coordination of cobalt substitution into host SnO_2 material without oxygen vacancy (upper-left), with oxygen vacancy (bottom-left), and zinc and cobalt with a vacancy adjacent to the cobalt relaxed in a $2 \times 2 \times 2$ SnO_2 crystal structure. The relaxed structures show warping of the tetrahedral coordination around the dopant atoms substituted into the lattice.

To investigate the distortions of the tetrahedral environment found, structural models of Co^{2+}–Sn^{4+} substitution, Co^{2+}–Sn^{4+} substitution with an adjacent oxygen vacancy to the substitution, and Co^{2+}/Zn^{2+}–Sn^{4+} substitution with a oxygen vacancy adjacent to the cobalt site were constructed, and relaxed using the process in Section 3.2 (Figure 3.2). This insertion of an oxygen vacancy follows the results of SnO_2 singly doped with Co, and to compensate for the valency difference between Co^{2+} and Sn^{4+} [69]. In Figure 3.1, the spectra produced from these models give good agreement, where the Co^{2+}–Sn^{4+} substitution displaying a shift in

features to lower energies in comparison to the Co^{2+}/Zn^{2+}–Sn^{4+} substitution. This suggests the distance between the cobalt and zinc dopants within the host SnO_2 lattice lies between these two cases, where the single doped cobalt case represents maximal separation.

This also confirms both the existence and proximity of oxygen vacancies to the cobalt sites and is a direct confirmation of the source of distortions on the tetragonal coordination.

The differences between experimentally measured spectra of samples with varying Cobalt and Zinc concentrations are less than the difference between the best fitting models in both those yielding crystal field splitting parameters and those generated using relaxed structural models. Therefore, conclusions can not be drawn for differing concentrations in samples using the Cobalt spectra.

3.3.2 Zn L edge

Figure 3.3 displays Zn $L_{2,3}$ XAS of the samples. Showing the second derivative of the $Sn_{0.90}Co_{0.05}Zn_{0.05}O_2$ and as synthesized $Sn_{0.85}Co_{0.075}Zn_{0.075}O_2$ samples' spectra, features are consistently pushed to lower energies after the annealing process.

Using the technique described in Section 3.2, XAS spectra modeled using DFT can be compared to experimental results. As synthesized samples show good agreement with a Zn^{2+}–Sn^{4+} model with a vacancy adjacent to the Zn^{2+} site. In addition, the energy shift seen in the onset of the annealed samples shows agreement with a Co^{2+}/Zn^{2+}–Sn^{4+} model with a vacancy adjacent to the Co^{2+} site. This, once again, shows direct evidence for not only the existence of oxygen vacancies within the material, but the precise location in adjacency to dopant atoms.

Similar to investigation in the Cobalt case, The differences between experimentally measured spectra of samples with varying Cobalt and Zinc concentrations are less than the difference between the best fitting model and the experimental spectra.

3.3.3 X-ray excited optical luminescence (XEOL)

X-ray excited optical luminescence (XEOL) measurements are complimentary to XAS measurements in investigating the effect of dopants on the band structure of a material. As-

synthesized samples display nominal luminescence, mirroring the results found of bulk SnO_2. Undoped annealed SnO_2 presents a strong resolved peak at $\sim$ 640 nm (1.93 eV). To investigate annealed $Sn_{0.95}Co_{0.025}Zn_{0.025}O_2$, a Gaussian deconvolution on the spectra (Figure S2) shows a redshift in the primary feature seen in the undoped annealed SnO_2 to $\sim$ 740 nm, and the emergence of a secondary feature at $\sim$ 550 nm. As dopant levels are increased in $Sn_{0.90}Co_{0.05}Zn_{0.05}O_2$, this secondary 740 nm feature disappears, and in $Sn_{0.85}Co_{0.075}Zn_{0.075}O_2$ the intensity of the 550 nm feature decreases. Since the band gap of SnO_2 is much larger than these luminescence values, neither can be attributed to a conduction band to valence band transition. These intragap defect states are in-line with prior results signifying the presence of oxygen vacancies within the material [57].

This suggests that with low concentrations of equal quantities of cobalt and zinc, oxygen vacancies are still produced. However a fraction of the material exists in a secondary defect state associated with oxygen defects in the original SnO_2 structure. Examining the other doped samples, there is an overall decreasing trend in luminescence intensity, excluding the $Sn_{0.90}Co_{0.05}Zn_{0.05}O_2$ case. In this case, the high overall luminescence intensity of the $Sn_{0.95}Co_{0.025}Zn_{0.025}O_2$ case is maintained, however the feature at $\sim$ 740 nm has disappeared. This suggests that the defect states seen in the annealed SnO_2 without dopants have been reduced.

The properties of transition-metal doped oxides are sensitively dependent on which sites transition metal ions occupy, where vacancies are distributed and their relative concentrations. We note that although there is no change in the nominal stoichiometry of our samples before and after annealing, in as-synthesized samples, no luminescence was observed in contrast with annealed samples. This can be explained by considering the differences in how the vacancies are distributed in the as-synthesized and annealed samples. In as-synthesized samples, the zinc atoms have adjacent vacancies, as seen in the Zn L-edge XAS experimental spectra and DFT calculations (Figure 3.3). The agreement between experiment and a calculation which neglects to include a cobalt atom suggests high separation distance and low interaction between cobalt and zinc atoms within the host SnO_2. This is in agreement with the fact that the Co L-edge spectra can be explained by a DFT calculated structure which does not include Zn atoms. Therefore, the relaxation of the cobalt cations into the SnO_2

during annealing facilitates a low interaction between cobalt and zinc atoms, and an optimal coordination for magnetic interactions [14].

In the annealed samples, the Co atoms have a single adjacent vacancy (determined via Co L-edge measurements), suggesting that the oxygen vacancy migrates adjacent to a Co atom during the annealing process. This is supported by the experimental Zn L-edge XAS spectra, which show clear changes when compared to the as-synthesized samples, and the absence of a vacancy prior to annealing seen in Figure A.1. Calculations of cells which include both Co and Zn dopants as well as vacancies provide somewhat more ambiguous agreement with annealed samples.

Having established the defect distribution for this system, and that the interaction between Co and Zn is weak, we are now able explain the absence of luminescence in the pre-annealed samples by considering the band structure of SnO_2 with a Zn atom and an adjacent oxygen vacancy. An energy momentum diagram of SnO_2, a SnO_2 with a vacancy and SnO_2 with a Zn atom and an adjacent vacancy is shown in Figure 3.5 in the left, middle and right panels, respectively. In pure SnO_2 no mid-gap states are observed. When a vacancy is introduced, the valence band is perturbed by the addition of a dispersive mid-gap band appears just above the top of the valence band and extends deep into the mid-gap region. The Fermi energy level is at the top of this band. Upon injecting carriers, electrons will reach a quasi-equilibrium in valleys at the bottom of the conduction band while holes will migrate to local maxima in the mid-gap band. These carriers can then recombine in momentum conserving transitions such as those indicated by arrows in the figure. The energy-momentum diagram for Zn with an adjacent vacancy is quite different. In this case, an additional band appears at the top of the valence band, but no new mid-gap states appear, which are required to mediate luminescence in the optical region.

3.3.4 Magnetic Properties

Field dependent magnetic measurements of as-synthesized and annealed samples at room temperature (300 K) were discussed in the earlier reports [10]. As-synthesized undoped SnO_2 exhibited diamagnetic nature. The as-synthesized $Sn_{0.95}Co_{0.025}Zn_{0.025}O_2$, $Sn_{0.925}Co_{0.05}Zn_{0.025}O_2$, $Sn_{0.925}Co_{0.025}Zn_{0.05}O_2$, $Sn_{0.90}Co_{0.05}Zn_{0.05}O_2$, and $Sn_{0.85}Co_{0.075}Zn_{0.075}O_2$

samples exhibited room temperature ferromagnetism (RTFM). The high saturation magnetization of 55.03×10^{-3} emu/g was observed for the as-synthesized $Sn_{0.85}Co_{0.075}Zn_{0.075}O_2$.

Interestingly, the annealed undoped SnO_2 exhibited RTFM with reasonable hysteresis loop, which can be attributed to oxygen vacancies as observed in Section 3.3.3. This follows the enhanced saturation magnetism of the RTFM found in the annealed samples as compared to the as-synthesized samples and links the RTFM to the Co–Zn interaction within the SnO_2 lattice. While zinc XAS spectra and DFT calculations indicate low interaction between the cobalt and zinc ions, with increasing concentration of dopants, the Co–Co separation distance decreases reaching an optimal coordination for ferromagnetic interactions. The improved crystallinity and the relaxation of the cobalt ions to this coordination along with the adjacent oxygen vacancies to the cobalt ions and the low interaction between cobalt and zinc ions facilitates the enhanced saturation magnetism.

3.4 Conclusion

We have investigated the local structure of Zn and Co co-dopants in SnO_2 samples with a variety of x-ray techniques, in addition to DFT and multiplet methodologies. We find that both Zn and Co atoms substitute Sn atoms within the bulk of the lattice, and attribute the ferromagnetic properties to oxygen vacancy mediated substitution of Co and Zn within the host lattice. Furthermore, we identify a secondary defect state within low concentration samples only appearing after annealing that disappears with concentrations of 5% Co and 5% Zn. Through this, we provide direct experimental evidence for the location and behavior of oxygen vacancies within a co-doped DMS system under annealing, and connect this to observed luminescence. In addition to this, the increased saturation magnetism in samples with increased dopant percentages can be attributed to the decreasing distance between Co atoms and associated cobalt-adjacent oxygen vacancies within the lattice.

The combination of synchrotron x-ray based experimental and theoretical techniques allows a link between observed magnetism and dopant–atom interactions within a host crystal. We display a novel methodology for usage of both density functional and multiplet theories for the modeling of DMS systems that proves effective in directly linking oxygen vacancies

and host lattice interactions with observed ferromagnetic properties.

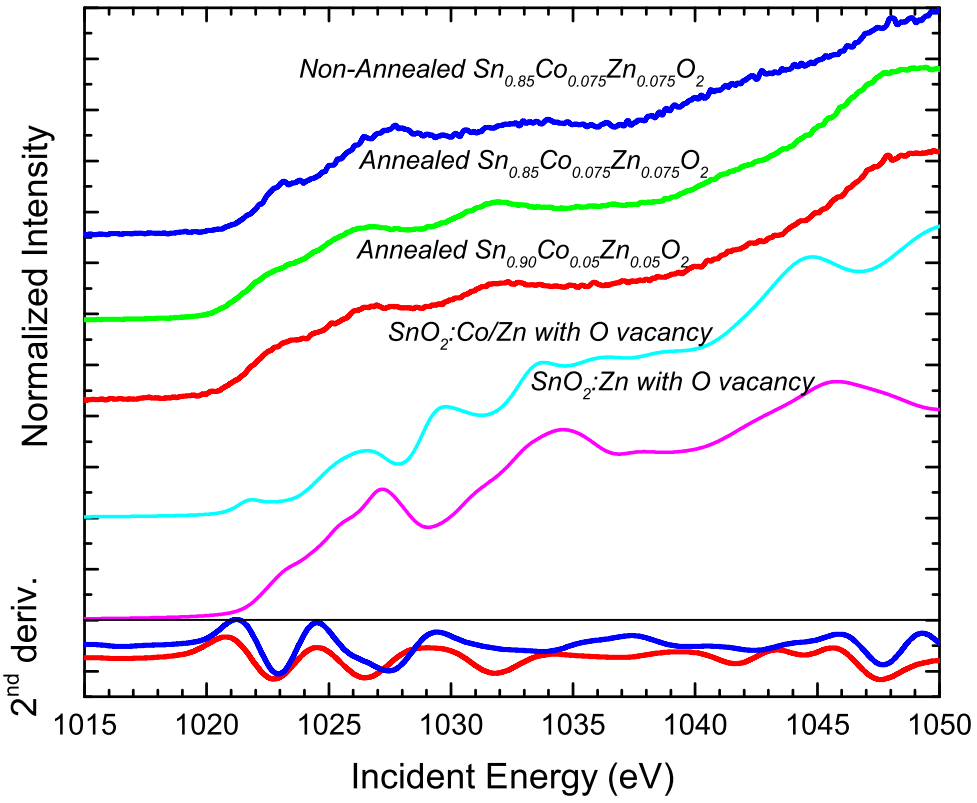

Figure 3.3: Zn $L_{2,3}$ XAS for annealed SnO_2 samples with as-synthesized $Sn_{0.85}Co_{0.075}Zn_{0.075}O_2$, second derivative for $Sn_{0.90}Co_{0.05}Zn_{0.05}O_2$ and as-synthesized $Sn_{0.85}Co_{0.075}Zn_{0.075}O_2$ shown at the bottom, and DFT models in cyan and magenta. In the second derivative, the decrease in onset energy between the "as-synthesized" and the annealed samples is clear, showing the shift from zinc adjacent oxygen vacancies to cobalt adjacent oxygen vacancies.

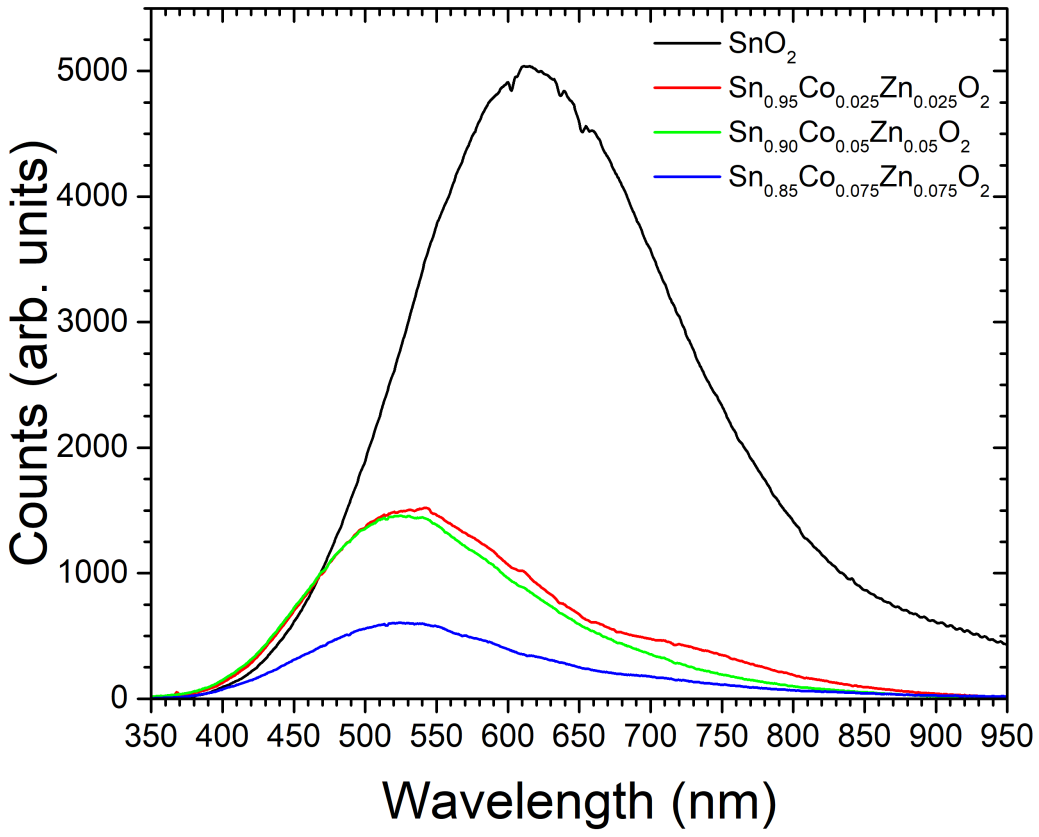

Figure 3.4: XEOL spectra for annealed SnO_2 samples. Undoped SnO_2 (black) is seen with a distinct peak at $\sim$ 620 nm, and doped SnO_2 consistently show a feature centered at $\sim$ 550 nm. A second feature is visible in the doped 2.5% Co, 2.5% Zn case (red). This clearly shows the shift of mid-gap defects from the inherent SnO_2 oxygen vacancies to a secondary defect caused by TM doping.

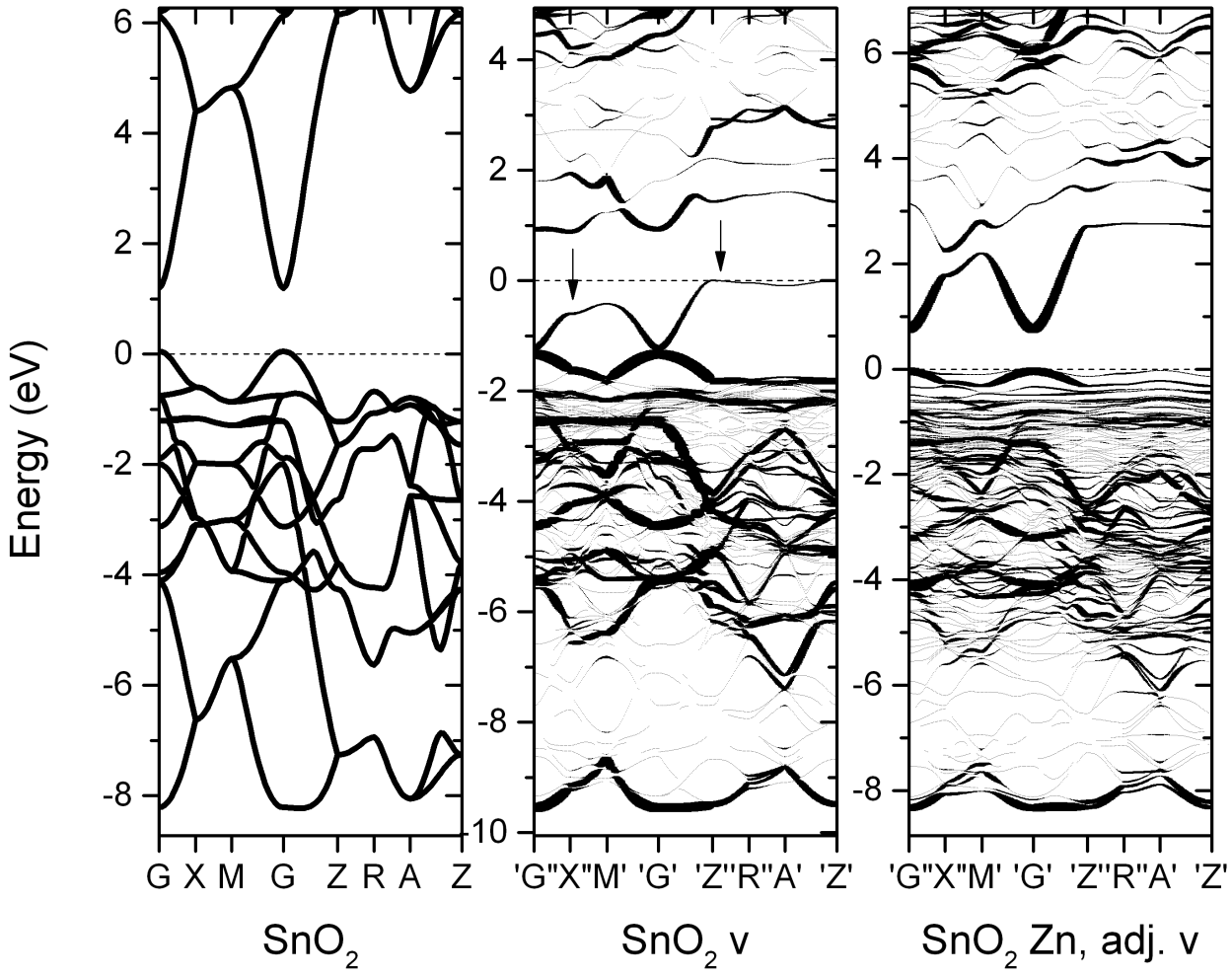

Figure 3.5: Band structure diagrams of SnO_2 calculated for a 2x2x2 SnO_2 unit cell with an oxygen vacancy and a 2x2x2 SnO_2 unit cell with a Zinc atom with an adjacent oxygen vacancy (labeled "adj. v") for a path in the original unit cell Brillouin zone. For the supercell band structures, the point size corresponds to the Bloch spectral weight.

Chapter 4

Conclusion

The focus of this thesis was to drive the understanding and development of spintronic materials. Furthermore, we refined our focus to be DMS systems. This brought us to two materials, In_2O_3 doped with manganese, cobalt, iron, and nickel and SnO_2 codoped with cobalt and zinc.

Our In_2O_3 system allowed a systematic study of one host material with multiple dopants. By utilizing complimentary multiplet calculations, the local bonding environment of the system was determined, and the interstitial, substitutional, and clustering states determined. While only the In_2O_3:Fe system proved to have significant substitutional states necessary for spintronic systems with the absence of interstitial or clustering states, the negative results of the other three dopant states proves important due to the widespread usage of ion implantation for doping.

The second system, based on SnO_2, proved an exciting arena to investigate the often discussed phenomenon of oxygen vacancies and more specifically, their connection to magnetic properties. With zinc and cobalt codopants, this created the interesting case of multiple potential oxygen vacancy sites adjacent to dopant atoms. Examining the data, the importance of the location of the oxygen vacancy, either adjacent to a zinc atom or a cobalt atom became evident. Furthermore, this location was controllable for the system using the simple technique of annealing where the oxygen vacancy was zinc-adjacent prior to high temperature annealing, and cobalt-adjacent after high temperature annealing.

4.1 Future Work

The understanding of synthesis techniques and methodology and their role in consistent spintronic materials is one of the crucial steps towards real-world spintronic devices. During our systematic investigation of In_2O_3, the results of different dopants on a single synthesis method and host material were demonstrated. Doing these kinds of studies is necessary and bring the understanding necessary to see the potentially world-changing devices that have been proposed.

In addition, the phenomenon of oxygen vacancies is only just beginning to unfold. These defect states, while often cited, are still relatively young in their understanding. As the understanding of defects within spintronic devices increases, not the least of these being oxygen vacancies, the remaining mysteries seen in spintronics and DMS systems can begin to be resolved.

Finally, our investigations herein greatly progressed the interfacing of DFT and crystal field multiplet calculations for the modelling of defect-inclusive systems. New techniques for refining structural modelling that can be used in conjunction with experimentally obtained spectra have been demonstrated, bolstering current crystal field methodology that has been utilized for many years. Going forward, this link between DFT and crystal field methodologies can be explored further to try and provide better and better approximations for the impurity-based models used here and towards a strong structure-based modelling for highly correlated systems like the $3d$ transition metals.

References

[1] Andrew Zangwill. *Physics at Surfaces*. Cambridge University Press, March 1988.

[2] B. L. Henke, E. M. Gullikson, and J. C. Davis. X-Ray Interactions: Photoabsorption, Scattering, Transmission, and Reflection at E = 50-30,000 eV, Z = 1-92. *Atomic Data and Nuclear Data Tables*, 54(2):181–342, July 1993.

[3] National Research Council. *Harnessing Light: Optical Science and Engineering for the 21st Century*. The National Academies Press, Washington, DC, December 1969.

[4] Anders Andrae. Total Consumer Power Consumption Forecast, October 2017.

[5] Cisco. Cisco Visual Networking Index: Forecast and Methodology, 2016–2021. Technical Report 146527200166118, February 2017.

[6] D. Salzman. Spintronic optical device, August 2002. US20020114032A1.

[7] D. Salzman. Spintronic optical shutter, April 2002. US20020044353A1.

[8] Adel S. Sedra and Kenneth C. Smith. *Microelectronic Circuits*. Oxford University Press, New York ; Oxford, seventh edition edition, November 2014.

[9] K. P. O'Donnell and X. Chen. Temperature dependence of semiconductor band gaps. *Appl. Phys. Lett.*, 58(25):2924–2926, June 1991.

[10] M. Tanaka. Ferromagnet/semiconductor hybrid structures grown by molecular-beam epitaxy. *J. of Cryst. Growth*, 201-202:660–669, May 1999.

[11] J. Halpern, S. Sinex, and S. Johnson. Chemistry: The Central Science (via LibreTexts), November 2014.

[12] H. Ohno. Making Nonmagnetic Semiconductors Ferromagnetic. *Science*, 281(5379):951–956, August 1998.

[13] R. J. Green, T. Z. Regier, B. Leedahl, J. A. McLeod, X. H. Xu, G. S. Chang, E. Z. Kurmaev, and A. Moewes. Adjacent Fe-Vacancy Interactions as the Origin of Room Temperature Ferromagnetism in $(In_{1-x}Fe_x)_2O_3$. *Phys. Rev. Lett.*, 115(16):167401, October 2015.

[14] Igor Djerdj, Zvonko Jagličić, Denis Arčon, and Markus Niederberger. Co-Doped ZnO nanoparticles : Minireview. *Nanoscale*, 2(7):1096–1104, 2010.

[15] M. A. Garcia, E. Fernandez Pinel, J. de la Venta, A. Quesada, V. Bouzas, J. F. Fernández, J. J. Romero, M. S. Martín González, and J. L. Costa-Krämer. Sources of experimental errors in the observation of nanoscale magnetism. *J. Appl. Phys.*, 105(1):013925, January 2009.

[16] Y. Nishi and R. Doering. *Handbook of Semiconductor Manufacturing Technology*. CRC Press, December 2017.

[17] J. Ziegler, M. Ziegler, and J. Biersack. SRIM - The stopping and range of ions in matter (2010). *Nucl. Instrum. Methods Phys. Res., Sect. B*, 268:1818–1823, June 2010.

[18] A. Lu, E. L. Salabas, and F. Schüth. Magnetic Nanoparticles: Synthesis, Protection, Functionalization, and Application. *Angew. Chem. Int. Ed.*, 46(8):1222–1244, February 2007.

[19] A. Achkar. *Inverse Partial Fluorescence Yield Spectroscopy*. PhD Thesis, University of Waterloo, Canada, August 2011.

[20] L. Liu and T. K. Sham. The Effect of Thermal Oxidation on the Luminescence Properties of Nanostructured Silicon. *Small*, 8(15):2371–2380, August 2012.

[21] Zhiqiang Wang, Chunlei Li, Lijia Liu, and Tsun-Kong Sham. Probing defect emissions in bulk, micro- and nano-sized α-Al_2O_3 via X-ray excited optical luminescence. *J. Chem. Phys.*, 138(8):084706, February 2013.

[22] P. Tola, A. Retournard, J. Dexpert-Ghys, M. Lemonnier, M. Pagel, and J. Goulon. On the use of x-ray-excited optical luminescence (XEOL) for the analysis of multisite rare-earth systems. *Chem. Phys.*, 78(3):339–345, August 1983.

[23] F. M. F. de Groot, J. C. Fuggle, B. T. Thole, and G. A. Sawatzky. 2p x-ray absorption of 3d transition-metal compounds: An atomic multiplet description including the crystal field. *Phys. Rev. B*, 42(9):5459–5468, September 1990.

[24] I. Žutic, J. Fabian, and S. Das Sarma. Spintronics: Fundamentals and applications. *Rev. Mod. Phys.*, 76(2):323–410, April 2004.

[25] J. M. D. Coey, M. Venkatesan, and C. B. Fitzgerald. Donor impurity band exchange in dilute ferromagnetic oxides. *Nat. Mater.*, 4(2):173–179, 2005.

[26] T. Dietl, H. Ohno, F. Matsukura, J. Cibert, and D. Ferrand. Zener Model Description of Ferromagnetism in Zinc-Blende Magnetic Semiconductors. *Science*, 287(5455):1019–1022, 2000.

[27] T. Dietl. Ferromagnetic semiconductors. *Semicond. Sci. Technol.*, 17(4):377, 2002.

[28] T. Ohno, T. Kawahara, H. Tanaka, T. Kawai, M. Oku, K. Okada, and S. Kohiki. Ferromagnetism in Transparent Thin Films of Fe-Doped Indium Tin Oxide. *Jpn. J. Appl. Phys.*, 45(9L):L957, 2006.

[29] Jun He, Shifa Xu, Young K. Yoo, Qizhen Xue, Hyung-Chul Lee, Shifan Cheng, X.-D. Xiang, Gerald F. Dionne, and Ichiro Takeuchi. Room temperature ferromagnetic n-type semiconductor in $(In_{1-x}Fe_x)_2O_{3-\sigma}$. *Appl. Phys. Lett.*, 86(5):052503, 2005.

[30] Y. K. Yoo, Q. Xue, H. C. Lee, S. Cheng, X.-D. Xiang, G. F. Dionne, S. Xu, J. He, Y. S. Chu, S. D. Preite, S. E. Lofland, and I. Takeuchi. Bulk synthesis and high-temperature ferromagnetism of $(In_{1-x}Fe_x)_2O_{3-\sigma}$ with Cu co-doping. *Appl. Phys. Lett.*, 86(4):042506, 2005.

[31] Z. G. Yu, J. He, S. Xu, Q. Xue, O. M. J. van't Erve, B. T. Jonker, M. A. Marcus, Y. Yoo, S. Cheng, and X. D. Xiang. Origin of ferromagnetism in semiconducting $(In_{1-x-y}Fe_xCu_y)_2O_{3-\sigma}$. *Phys. Rev. B*, 74(16):165321, October 2006.

[32] J. Philip, A. Punnoose, B. I. Kim, K. M. Reddy, S. Layne, J. O. Holmes, B. Satpati, P. R. LeClair, T. S. Santos, and J. S. Moodera. Carrier-controlled ferromagnetism in transparent oxide semiconductors. *Nat. Mater.*, 5(4):298–304, 2006.

[33] S. Khatoon, K. Coolahan, S. E. Lofland, and T. Ahmad. Solvothermal Synthesis of $In_{2-x}Co_xO_3$ ($0.05 \leq x \leq 0.15$) Dilute Magnetic Semiconductors: Optical, Magnetic, and Dielectric Properties. *Journal of the American Ceramic Society*, 96(8):2544–2550, August 2013.

[34] Tokeer Ahmad, Sarvari Khatoon, and Kelsey Coolahan. Synthesis, magnetic and dielectric characterization of nanocrystalline solid solutions of $In_{2-x}Ni_xO_3$ (x=0.05, 0.10 and 0.15). *Mater. Res. Bull.*, 48(9):3065–3071, September 2013.

[35] A. M. H. R. Hakimi, M. G. Blamire, S. M. Heald, Marzook S. Alshammari, M. S. Alqahtani, D. S. Score, H. J. Blythe, A. M. Fox, and G. A. Gehring. Donor-band ferromagnetism in cobalt-doped indium oxide. *Phys. Rev. B*, 84(8):085201, August 2011.

[36] X. Li, C. Xia, G. Pei, and X. He. Synthesis and characterization of room-temperature ferromagnetism in Fe- and Ni-co-doped In_2O_3. *J. Phys. Chem. Solids*, 68(10):1836–1840, October 2007.

[37] Y. An, S. Wang, D. Feng, Z. Wu, and J. Liu. Correlation between oxygen vacancies and magnetism in Fe-doped In_2O_3 films. *Appl. Surf. Sci.*, 276:535–538, July 2013.

[38] G. Korotcenkov, V. Brinzari, A. Cerneavschi, A. Cornet, J. Morante, A. Cabot, and J. Arbiol. Crystallographic characterization of In_2O_3 films deposited by spray pyrolysis. *Sens. Actuators, B*, 84(1):37 – 42, 2002.

[39] G. Korotcenkov, V. Brinzari, A. Cerneavschi, M. Ivanov, V. Golovanov, A. Cornet, J. Morante, A. Cabot, and J. Arbiol. The influence of film structure on In_2O_3 gas response. *Thin Solid Films*, 460(1–2):315 – 323, 2004.

[40] M. Boots, D. Muir, and A. Moewes. Optimizing and characterizing grating efficiency for a soft X-ray emission spectrometer. *J. Synchrotron Radiat.*, 20(2):272–285, March 2013.

[41] T. Regier, J. Krochak, T. K. Sham, Y. F. Hu, J. Thompson, and R. I. R. Blyth. Performance and capabilities of the Canadian Dragon: The SGM beamline at the Canadian Light Source. *Nucl. Instrum. Methods Phys. Res., Sect. A*, 582(1):93–95, November 2007.

[42] R. Qiao, Q. Li, Z. Zhuo, S. Sallis, O. Fuchs, M. Blum, L. Weinhardt, C. Heske, J. Pepper, M. Jones, A. Brown, A. Spucces, K. Chow, B. Smith, P. Glans, Y. Chen, S. Yan, F. Pan, L. F. J. Piper, J. Denlinger, J. Guo, Z. Hussain, Y. Chuang, and W. Yang. High-efficiency in situ resonant inelastic x-ray scattering (iRIXS) endstation at the Advanced Light Source. *Rev. Sci. Instrum.*, 88(3):033106, March 2017.

[43] J. Soler, E. Artacho, J. D. Gale, A. García, J. Junquera, P. Ordejón, and D. Sánchez-Portal. The SIESTA method for ab initio order-N materials simulation. *J. Phys.: Condens. Matter*, 14(11):2745, 2002.

[44] J. Perdew, K. Burke, and M. Ernzerhof. Generalized Gradient Approximation Made Simple. *Phys. Rev. Lett.*, 77(18):3865–3868, October 1996.

[45] N. Troullier and José Luís Martins. Efficient pseudopotentials for plane-wave calculations. *Phys. Rev. B*, 43(3):1993–2006, January 1991.

[46] H. J. Monkhorst and J. D. Pack. Special points for Brillouin-zone integrations. *Phys. Rev. B*, 13(12):5188–5192, June 1976.

[47] Robert D. Cowan. Theoretical Calculation of Atomic Spectra Using Digital Computers. *J. Opt. Soc. Am.*, 58(6):808–818, June 1968.

[48] M. W. Haverkort, G. Sangiovanni, P. Hansmann, A. Toschi, Y. Lu, and S. Macke. Bands, resonances, edge singularities and excitons in core level spectroscopy investigated within the dynamical mean-field theory. *Europhys. Lett.*, 108(5):57004, 2014.

[49] Maurits Haverkort. *Spin and orbital degrees of freedom in transition metal oxides and oxide thin films studied by soft x-ray absorption spectroscopy*. PhD Thesis, University of Cologne, Germany, 2005.

[50] B. Leedahl, D. A. Zatsepin, D. W. Boukhvalov, E. Z. Kurmaev, R. J. Green, I. S. Zhidkov, S. S. Kim, L. Cui, N. V. Gavrilov, S. O. Cholakh, and A. Moewes. Study of the Structural Characteristics of 3d Metals Cr, Mn, Fe, Co, Ni, and Cu Implanted in ZnO and TiO_2–Experiment and Theory. *J. Phys. Chem. C*, 118(48):28143–28151, 2014.

[51] E. Z. Kurmaev, A. L. Ankudinov, J. J. Rehr, L. D. Finkelstein, P. F. Karimov, and A. Moewes. The L2:L3 intensity ratio in soft X-ray emission spectra of 3d-metals. *J. Electron. Spectrosc. Relat. Phenom.*, 1(148):1–4, 2005.

[52] K. Nomura, J. Okabayashi, K. Okamura, and Y. Yamada. Magnetic properties of Fe and Co codoped SnO_2 prepared by sol-gel method. *J. Appl. Phys.*, 110(8):083901, October 2011.

[53] J. Kaur, J. Shah, R.K. Kotnala, and K. Verma. Raman spectra, photoluminescence and ferromagnetism of pure, Co and Fe doped SnO_2 nanoparticles. *Ceram. Int.*, 38(7):5563–5570, September 2012.

[54] J. Hays, A. Punnoose, R. Baldner, M. H. Engelhard, J. Peloquin, and K. M. Reddy. Relationship between the structural and magnetic properties of Co-doped SnO_2 nanoparticles. *Phys. Rev. B*, 72(7):075203, August 2005.

[55] E. Selvi and S. Sundar. Effect of replacing Sn^{4+} ions by Zn^{2+} ions on structural, optical and magnetic properties of SnO_2 nanoparticles. *Appl. Phys. A*, 123(5):383, April 2017.

[56] Y. Fu, N. Sun, L. Feng, S. Wen, Y. An, and J. Liu. Local structure and magnetic properties of Fe-doped SnO_2 films. *J. Alloys Compd.*, 698:863–867, March 2017.

[57] M. García-Tecedor, D. Maestre, A. Cremades, and J. Piqueras. Influence of Cr Doping on the Morphology and Luminescence of SnO_2 Nanostructures. *J. Phys. Chem. C*, 120(38):22028–22034, September 2016.

[58] X. Liu, J. Iqbal, Z. Wu, B. He, and R. Yu. Structure and Room-Temperature Ferromagnetism of Zn-Doped SnO_2 Nanorods Prepared by Solvothermal Method. *J. Phys. Chem. C*, 114(11):4790–4796, March 2010.

[59] J. Okabayashi, S. Kono, Y. Yamada, and K. Nomura. Magnetic and electronic properties of Fe and Ni codoped SnO_2. *J. Appl. Phys.*, 112(7):073917, October 2012.

[60] H. Katayama-Yoshida, T. Nishimatsu, T. Yamamoto, and N. Orita. Codoping method for the fabrication of low-resistivity wide band-gap semiconductors in p-type GaN, p-type AlN and n-type diamond: prediction versus experiment. *J. Phys.: Condens. Matter*, 13(40):8901, 2001.

[61] D. Manikandan and R. Murugan. Room temperature dilute magnetism in nanoscale Co and Zn co-doped SnO_2. *Superlattices Microstruct.*, 89:7–14, January 2016.

[62] K. Schwarz and P. Blaha. Solid state calculations using WIEN2k. *Computational Materials Science*, 28(2):259–273, October 2003.

[63] John P. Perdew, Adrienn Ruzsinszky, Gábor I. Csonka, Oleg A. Vydrov, Gustavo E. Scuseria, Lucian A. Constantin, Xiaolan Zhou, and Kieron Burke. Restoring the Density-Gradient Expansion for Exchange in Solids and Surfaces. *Phys. Rev. Lett.*, 100(13):136406, April 2008.

[64] A. A. Bolzan, C. Fong, B. J. Kennedy, and C. J. Howard. Structural Studies of Rutile-Type Metal Dioxides. *Acta Crystallogr., Sect. B*, 53(3):373–380.

[65] K. Schwarz, A. Neckel, and J. Nordgren. On the X-ray emission spectra from FeAl. *J. Phys. F: Met. Phys.*, 9(12):2509, 1979.

[66] Y. Hinuma, G. Pizzi, Y. Kumagai, F. Oba, and I. Tanaka. Band structure diagram paths based on crystallography. *Comput. Mater. Sci*, 128:140–184, 2017.

[67] O. Rubel, A. Bokhanchuk, S. J. Ahmed, and E. Assmann. Unfolding the band structure of disordered solids: From bound states to high-mobility Kane fermions. *Phys. Rev. B*, 90(11):115202, September 2014.

[68] E. Antonides, E. C. Janse, and G. A. Sawatzky. LMM auger spectra of Cu, Zn, Ga, and Ge. I. Transition probabilities, term splittings, and effective Coulomb interaction. *Phys. Rev. B*, 15(4):1669–1679, February 1977.

[69] H. Wang, Y. Yan, Y. Sh. Mohammed, X. Du, K. Li, and H. Jin. First-principle study of magnetism in Co-doped SnO_2. *J. Magn. Magn. Mater.*, 321(5):337–342, March 2009.

Appendix

Additional Figures

A.1 As Synthesized Co L Edge

While the annealed and as synthesized $Sn_{0.925}Co_{0.075}Zn_{0.075}O_2$ samples are similar in appearance, extracted crystal field parameters are significantly different. With $10Dq = -0.5$, $Ds = -0.2$, $Dt = -0.2$, and a Slater integral scaling of 55%, the tetrahedral symmetry indicated by the $10Dq$ is highly distorted shown by the nonzero Ds and Dt values. In addition to this, the Slater integral scaling of 55% suggests a non-optimal crystal structure for this configuration (Figure S1). Similarly, modeling using a cobalt substitution without an adjacent oxygen vacancy gives good agreement.

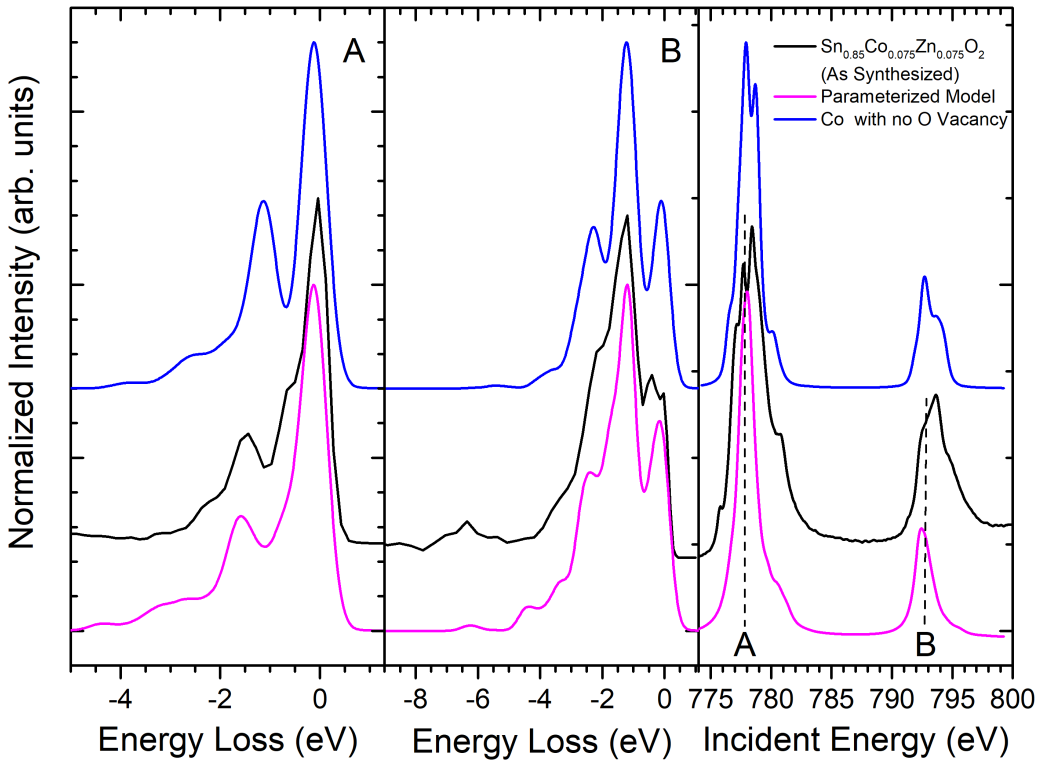

Figure A.1: Calculated spectra using a parameterized model (magenta), and a cobalt substitution with no oxygen vacancy for as synthesized $Sn_{0.925}Co_{0.075}Zn_{0.075}O_2$ samples.

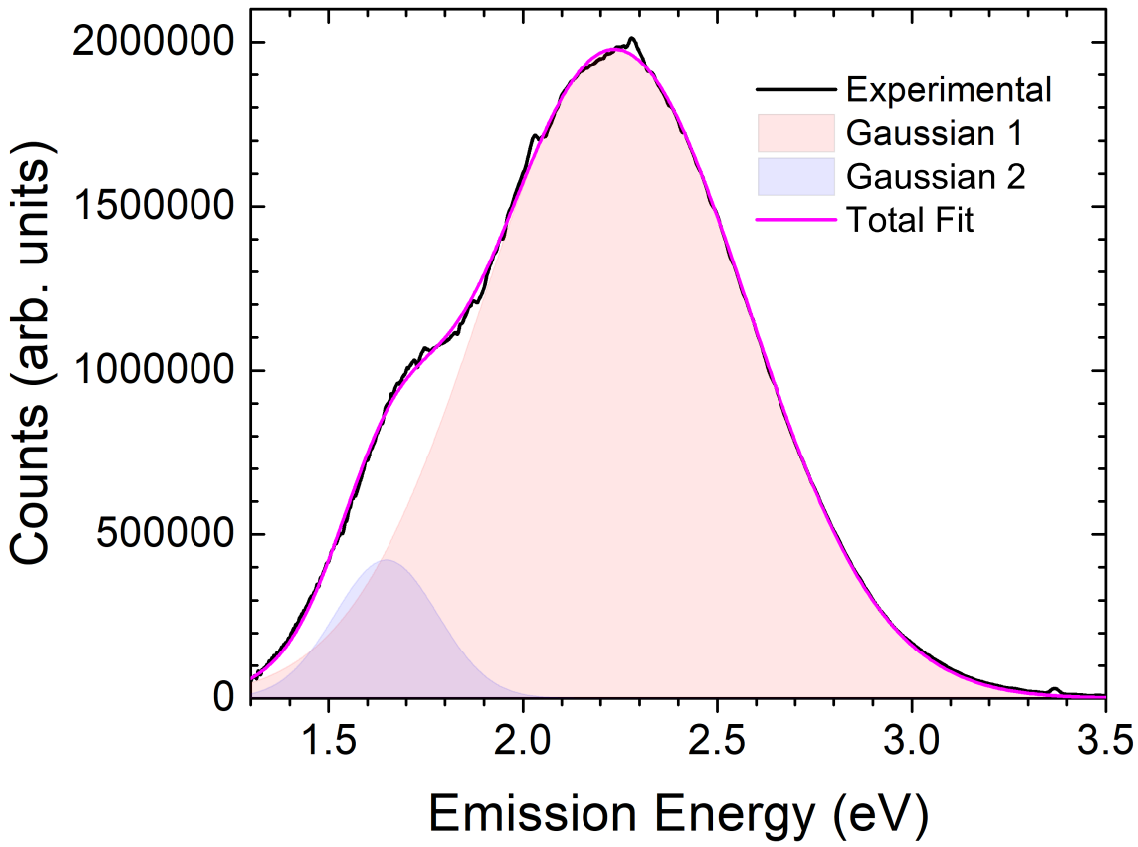

Figure A.2: XEOL spectra for annealed $Sn_{0.925}Co_{0.025}Zn_{0.025}O_2$ samples with gaussian deconvolution indicating two distinct luminescence features.

A.2 Gaussian Decomposition of XEOL

As discussed in the main text, gaussian decompositions were performed on collected XEOL spectra for all samples. XEOL spectra were collected on a wavelength scale, however rescaling the axis to an energy scale provides a more reliable result while investigating luminescence features. In Figure 4, two gaussian features are clearly seen within the spectra contrasting the other measured samples seen in Figure 4.